ANGLES-ONLY INITIAL ORBIT DETERMINATION: COMPARISON OF RELATIVE DYNAMICS AND INERTIAL DYNAMICS APPROACHES

Kenneth R. Horneman,[*] Alex E. Sizemore,[†] Bradyn W. Morton,[‡] T. Alan Lovell,[§] Brett A. Newman,[**] and Andrew J. Sinclair[††]

This paper investigates two classes of methods to determine the motion of a space object using line-of-sight measurements collected by a known space-based observer. The so-called "classical" initial orbit determination methods are typically applied to scenarios involving long baselines between the observer and the space object, such as an observer on Earth or an observer in a very different orbit from the space object. However, these methods are mathematically applicable to short baseline, i.e. close proximity, scenarios as well. By comparison, an initial relative orbit determination method has been developed primarily for close proximity scenarios. Thus, a comparison is warranted between and among the various classical initial orbit determination algorithms and the more recently developed initial relative orbit determination algorithm. This paper investigates such a comparison over a broad selection of simulated test cases. These cases encompass a variety of different space-based observer locations, as well as different space object orbits. Metrics of comparison include solution accuracy and line-of-sight residuals. In particular, the sensitivity of the various algorithms to measurement sample rate and separation between the observer and space object is explored.

INTRODUCTION

Angles-only initial orbit determination (IOD) enables the determination of a space object's orbit about a central body using a minimal number of line-of-sight (LOS) measurements, where the location of the observer at each measurement time is assumed known. This astrodynamics problem has been explored for many years, but is still a subject of ongoing research. The Gauss and Laplace methods are examples of classical IOD techniques (see, for example, References 1-3). These methods are based on the inertial dynamics of the space object (typically from a two-body gravitational perspective) and were developed primarily for tracking of space objects from ground-based sensors. However, since these methods only require the LOS measurements and

[*] Postdoctoral Research Associate, National Research Council.
[†] Graduate Student, Dept of Aerospace Engineering, University of Kansas.
[‡] Graduate Student, Dept of Aerospace Engineering, Missouri University of Science and Technology.
[§] Senior Aerospace Engineer, Air Force Research Laboratory.
[**] Professor, Old Dominion University.
[††] Senior Aerospace Engineer, Air Force Research Laboratory.

the observer location at each measurement time, they can be applied to scenarios involving space-based observers as well.

Recently, the growth of spacecraft missions involving formation flying, rendezvous, and proximity operations has motivated the study of angles-only IOD techniques based on the relative dynamics between the observer (or some reference orbit) and the space object. We will use the term initial relative orbit determination (IROD) to refer to these techniques. The relative approach allows the use of closed-form approximate solutions of the relative motion dynamics, such as linear or second-order models (e.g. Refs 4-8). This in turn allows the possibility of an IROD algorithm that, if not entirely closed-form, at least exhibits compactness and involves little to no iteration. Some initial studies involving IROD algorithms include Ref 9.

This paper will investigate short-baseline (close proximity) IOD utilizing several classical (inertial dynamics) methods as well as IROD (relative dynamics) algorithms. A number of simulated test cases will be chosen encompassing various space-based observer locations and space object orbits. Metrics of comparison include solution accuracy and LOS residuals. In particular, the sensitivity of the various algorithms to measurement sample rate and separation between the observer and space object will be explored.

It should be mentioned that every IOD/IROD solution computed in this paper is a "cold start" solution, i.e. no initial guess or other knowledge of the RSO orbit is required. Also, while some of these methods lend themselves to iterative refinement or correction of the original solution, no iteration was performed for this paper; i.e. each solution detailed in the results is the original solution obtained by the particular method. Ref 10, which can be considered a companion to this work, does in fact compare inertial dynamics-based and relative dynamics-based orbit determination techniques that involve differential corrections.

CLASSICAL IOD METHODS

The classical IOD techniques included in this study are the Gauss and Laplace methods. These methods are well known, and thus are only described briefly here. Both methods assume two-body gravitational motion. The inputs are the LOS vector from the observer to the space object at each of three measurement times, as well as the vector from the center of the attracting body to the observer at each measurement time. All vectors are expressed in an inertial frame. The output is the orbit of the space object, expressed in terms of inertial position and velocity vectors.

The Laplace method incorporates the "exact" two-body gravitational motion of the object along with a Lagrangian approximation of the LOS history and its derivative into a set of algebraic relationships. This leads to an 8^{th}-order polynomial whose independent variable is the range from the center of the attracting body to the object at the middle (2^{nd}) measurement time. After selecting the proper root of the polynomial, multiplying by the given LOS vector yields the inertial position vector of the object at the middle measurement time, and inserting this back into the original algebraic equations yields the inertial velocity vector at this time.

The Gauss method in some respect is the converse of the Laplace method, in that it incorporates the f and g series approximation of two-body motion but sets up geometric relationships such that the LOS constraints (according to f and g series dynamics) are exactly satisfied. Like Laplace, this method results in an 8^{th}-order polynomial for the range at the middle measurement time, which then yields the inertial position vector of the object at this time. One can then propagate forward and backward using f and g series to obtain the inertial position vector of the object at the other two measurement times, then use a method such as Gibbs or Herrick-Gibbs to obtain the inertial velocity vector given the three inertial position vectors.

RELATIVE MOTION DYNAMICS

Before introducing the IROD method, a brief discussion of relative motion dynamics is given, including certain closed-form relative motion solutions that exist.

An effective coordinate frame in which to characterize the motion of a "deputy" space object relative to a "chief" object is a Cartesian coordinate frame known as the local-vertical-local-horizontal (LVLH) frame. This frame entails defining a reference orbit about the Earth, defining the chief object on this orbit, and attaching a coordinate frame to the chief's center of mass. This is depicted in Figure 1. The LVLH coordinate directions are then defined as follows: the "x" or radial direction is aligned with the chief's inertial position vector (i.e. the vector from Earth's center to the chief), the "z" or cross-track direction is aligned with the chief's angular momentum vector (i.e. perpendicular to the chief's orbit plane), and the "y" direction is the cross product of z and x. (If the chief orbit is circular, the "y" direction is then aligned with the chief's inertial velocity vector and is often called along-track.) Note that the LVLH frame translates and rotates around the Earth with the chief object, therefore these directions are defined instantaneously. In this paper, we model the relative motion between the observer and a resident space object (RSO) in this frame.

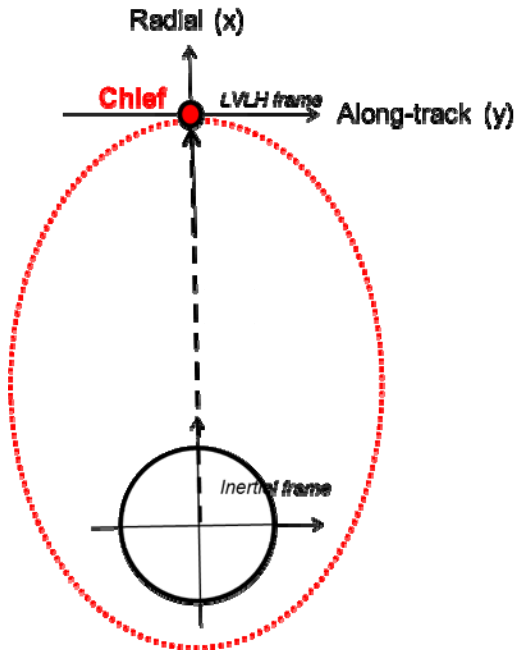

Figure 1. LVLH Coordinate Frame, with Chief Orbit and x and y Axis Directions Depicted, and z Axis Direction Going into the Page.

Clohessy-Wiltshire Solution

Probably the most well-known closed-form solution for relative motion is that of Clohessy and Wiltshire.[5] This solution assumes the chief orbit is circular and is commonly derived by writing the two-body differential equations of motion for both the chief and deputy, differencing these equations, and expanding the difference to first order in a Taylor series. The result is a set of linear time-invariant differential equations in LVLH coordinates whose solution is

$$
\begin{aligned}
x(t) &= \left[4-3\cos(nt)\right]x_0 + \frac{\dot{x}_0}{n}\sin(nt) + \frac{2}{n}\left[1-\cos(nt)\right]\dot{y}_0 \\
y(t) &= 6\left(\sin(nt)-nt\right)x_0 + y_0 + \frac{2}{n}\left[\cos(nt)-1\right]\dot{x}_0 + \left[\frac{4}{n}\sin(nt)-3t\right]\dot{y}_0 \\
z(t) &= \cos(nt)z_0 + \frac{1}{n}\sin(nt)\dot{z}_0
\end{aligned}
\tag{1}
$$

where n is the mean motion of the chief orbit. This yields the deputy's instantaneous relative position components in terms of the relative initial conditions. Differentiating these expressions with respect to time yields the relative velocity components.

Relative Orbit Elements

Relative Orbit Elements (ROEs) are a geometric description of relative motion between two space objects, termed the "chief" and "deputy." ROEs are analogous to classical orbital elements, which describe two-body inertial motion of a single object. The ROE formulation adopted here first appeared in Ref. 11 and later in Ref. 12. This particular ROE set serves as a re-parameterization of the Clohessy-Wiltshire solution, under which the motion can be generally described as a drifting 2x1 ellipse in the x-y (radial/along-track) plane, with sinusoidal motion in the z (cross-track) direction superposed. The conversion from Cartesian relative states $\left[x\ y\ z\ \dot{x}\ \dot{y}\ \dot{z}\right]^T$ to ROEs is as follows:

$$
\begin{aligned}
a_e &= 2\sqrt{\left(\frac{\dot{x}}{n}\right)^2 + \left(3x + 2\frac{\dot{y}}{n}\right)^2} \\
x_d &= 4x + 2\frac{\dot{y}}{n} \\
y_d &= y - 2\frac{\dot{x}}{n} \\
\beta &= \operatorname{atan2}\left(\dot{x}, 3nx + 2\dot{y}\right) \\
z_{\max} &= \sqrt{\left(\frac{\dot{z}}{n}\right)^2 + z^2} \\
\gamma &= \operatorname{atan2}\left(nz, \dot{z}\right) - \beta
\end{aligned}
\tag{2}
$$

where a_e is the length of the semimajor axis of the 2x1 ellipse, x_d is the radial distance of the center of the ellipse above or below the y (along-track) axis, y_d is the along-track distance of the center of the ellipse ahead or behind the x (radial) axis, β is the anomaly angle indicating the deputy's location in its relative orbit, z_{max} is the amplitude of the sinusoidal cross-track motion, and γ is the phase difference between the radial/along-track motion and cross-track motion. Under the assumptions of Clohessy-Wiltshire motion, a_e, x_d, z_{max}, and γ remain constant while β and y_d vary linearly with time. For real scenarios, this will not be the case, but it is still useful at any point in a scenario to convert the Cartesian relative states to ROEs in order to get an instantaneous "snapshot" of the geometry of the relative orbit.

Second-Order (Quadratic Volterra) Solution

Another closed-form relative motion solution is derived in Refs. 6-8. This solution is similar to the Clohessy-Wiltshire solution in that it assumes two-body gravity and a circular chief orbit. However, instead of retaining only terms linear in the initial relative states, it retains second-order terms as well. The solution for the *x* component of relative position in the LVLH frame is given as follows:

$$\begin{aligned} x(t) = {} & (4-3C(nt))x_0 + \frac{\dot{x}_0 S_{nt}}{n} + (1-C(nt))(\frac{2\dot{y}_0}{n}) + \frac{3x_0^2}{2R}(7-10C(nt)+3C(2nt)+12ntS(nt)-12n^2t^2) \\ & + \frac{3y_0^2}{2R}(1-C(nt)) + \frac{z_0^2}{4R}(3-2C(nt)-C(2nt)) + \frac{\dot{x}_0^2}{2Rn^2}(-3+4C(nt)-C(2nt)) \\ & + \frac{\dot{y}_0^2}{2Rn^2}(6-10C(nt)+4C(2nt)+12ntS(nt)-9n^2t^2) + \frac{\dot{z}_0^2}{4Rn^2}(3-4C(nt)+C(2nt)) \\ & + \frac{6x_0y_0}{R}(-S(nt)+nt) + \frac{3\dot{x}_0x_0}{Rn}(4S(nt)-S(2nt)-4nt+2ntC(nt)) \\ & + \frac{3\dot{y}_0x_0}{Rn}(4-6C(nt)+2C(2nt)+7ntS(nt)-6n^2t^2) + \frac{3\dot{y}_0y_0}{Rn}(-S(nt)+nt) + \frac{\dot{z}_0z_0}{2Rn}(2S(nt)-S(2nt)) \\ & + \frac{\dot{x}_0\dot{y}_0}{Rn^2}(7S(nt)-2S(2nt)-6nt+3ntC(nt)) \end{aligned} \tag{3}$$

where *R* is the (circular) chief orbit radius. The *y* and *z* components are similar in form. In Ref. 8 this solution is referred to as the "Quadratic Volterra" (QV) solution and will therefore be referred to as "QV" in this paper.

INITIAL RELATIVE ORBIT DETERMINATION

In this section, the concept of LOS (or angles-only) initial relative orbit determination is described. The LOS measurement equations are first derived, followed by a discussion of the observability issue arising in space-based OD scenarios, then a candidate IROD algorithm is laid out.

Derivation of Measurement Equations

Consider a measured LOS vector at time t_i expressed in the LVLH frame, i.e. $\hat{u}_r(t_i) = u_x(t_i)\hat{i} + u_y(t_i)\hat{j} + u_z(t_i)\hat{k}$. The measurement equations can be formed by requiring that the relative position vector is parallel to the LOS at each measurement time:

$$\hat{u}_r(t_i) \times \bar{r}(t_i) = U(t_i)\bar{r}(t_i) = \begin{bmatrix} 0 & -u_z(t_i) & u_y(t_i) \\ u_z(t_i) & 0 & -u_x(t_i) \\ -u_y(t_i) & u_x(t_i) & 0 \end{bmatrix} \bar{r}(t_i) = 0 \tag{4}$$

or

$$\begin{aligned} u_z(t_i)y(t_i) - u_y(t_i)z(t_i) &= 0 \\ u_z(t_i)x(t_i) - u_x(t_i)z(t_i) &= 0 \\ u_y(t_i)x(t_i) - u_x(t_i)y(t_i) &= 0 \end{aligned} \tag{5}$$

Note that the LOS components $u_x(t_i)$, $u_y(t_i)$, $u_z(t_i)$ are known, but the relative position states $x(t_i)$, $y(t_i)$, $z(t_i)$ are unknown. The relative position states at t_i can be related to the initial relative

states $\left[x_0\ y_0\ z_0\ \dot{x}_0\ \dot{y}_0\ \dot{z}_0\right]^T$ via a closed-form relative motion solution (e.g. one of the solutions cited above). This would yield three equations whose unknowns are the initial relative states. However, only two of the three equations in Eq. (5) are independent. Thus, if we obtain a LOS measurement at three specific times, choose two of the equations from Eq. (5) at each time, and employ a closed-form relative motion solution, we have a "square" system, i.e. six measurement equations from which to solve the six initial relative states $\left[x_0\ y_0\ z_0\ \dot{x}_0\ \dot{y}_0\ \dot{z}_0\right]^T$.

Observability

Suppose we follow the above procedure and choose as our closed-form relative motion solution a linear solution such as the Clohessy-Wiltshire solution. We can then write the solution in the form of a state-transition matrix $\Phi(t_i, t_0)$ and can relate the relative position vector at t_i to the initial state vector using elements of the state-transition matrix:

$$\bar{r}(t_i) = \left[x(t_i) \quad y(t_i) \quad z(t_i)\right]^T = \left[\Phi_{rr}(t_i, t_0) \quad \Phi_{rv}(t_i, t_0)\right]\bar{x}_0 \tag{6}$$

where $\bar{x}_0$ represents the six initial relative states $\left[x_0\ y_0\ z_0\ \dot{x}_0\ \dot{y}_0\ \dot{z}_0\right]^T$ and $\Phi_{rr}(t_i, t_0)$ and $\Phi_{rv}(t_i, t_0)$ represent the upper left and upper right 3x3 submatrices of $\Phi(t_i, t_0)$, respectively. Inserting Eq. (5) into Eq. (3) yields

$$\begin{bmatrix} 0 & -u_z(t_i) & u_y(t_i) \\ u_z(t_i) & 0 & -u_x(t_i) \\ -u_y(t_i) & u_x(t_i) & 0 \end{bmatrix}\left[\Phi_{rr}(t_i, t_0) \quad \Phi_{rv}(t_i, t_0)\right]\bar{x}_0 = 0 \tag{7}$$

These are linear equations in $\bar{x}_0$. Again, only two of the three equations are independent, so if we obtain three LOS measurements, choosing two of the measurement equations at each time, this yields a system of the form $A\bar{x}_0 = 0$, where A is a 6x6 matrix whose elements are known.

If there exists a nonzero solution $\bar{x}_0^*$ to this system, then $\alpha\bar{x}_0^*$ is a solution as well, where α is any positive real value. This implies an infinite number of relative orbits corresponding to a given set of LOS measurements; in fact, these relative orbits don't just possess the same LOS values at specific measurement times, but in fact for all time. Physically, this can be thought of as "range ambiguity," as depicted in Figure 2 (where the Clohessy-Wiltshire solution is used to propagate the relative motion). Each plot shows a manifold or "family" of multiple trajectories possessing an initial state of the form $\alpha\bar{x}_0^*$. For each manifold, the trajectories share the same $\bar{x}_0^*$, but each trajectory corresponds to a different value of α. From an IROD perspective, it is possible that in a particular scenario $\bar{x}_0^*$ can be determined, but the specific "size" or scale factor α of the trajectory cannot be determined. This scenario of guaranteed infinite ambiguity will be referred to as "Woffinden's Dilemma" because it was first described in Ref. 13. Note that this

guaranteed ambiguity is not a function of how many measurements are taken; i.e., one cannot somehow create observability by taking more measurements.

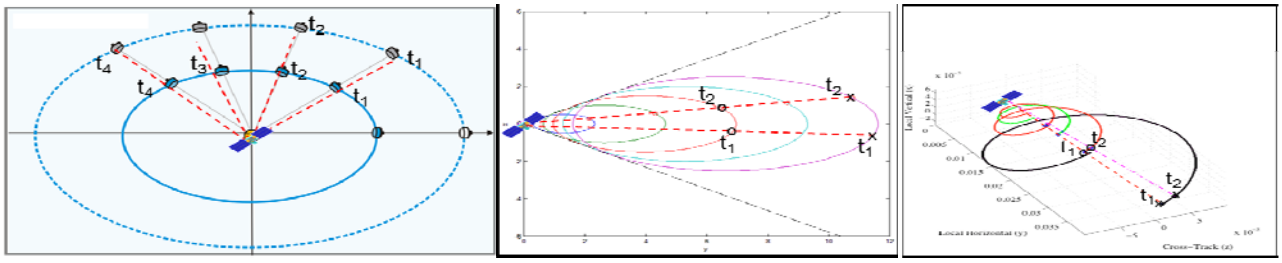

Figure 2. Representation of a "family" of ambiguous relative orbits, as seen by a space-based observer (Figure 2a: circumnavigation orbits, Figure 2b: offset orbits, Figure 2c: 3-D drifting orbits).

It is instructive to explore how "Woffinden's Dilemma" affects ROE values. As was done in a previous section, consider two trajectories, one whose values at t_0 are given by $\bar{x}_{01}$ and the other whose initial values are $\bar{x}_{02} = \alpha\bar{x}_{01}$, where α is a positive real number. At this instant, the values of a_e for the two trajectories (call them a_{e1} and a_{e2}) are related by

$$a_{e2} = 2\sqrt{\left(\frac{\dot{x}_2}{n}\right)^2 + \left(3x_2 + 2\frac{\dot{y}_2}{n}\right)^2} = 2\sqrt{\left(\frac{\alpha\dot{x}_1}{n}\right)^2 + \left(3\alpha x_1 + 2\frac{\alpha\dot{y}_1}{n}\right)^2} = \alpha a_{e1} \tag{8}$$

Thus we see that a_e scales with α. It can also be shown from the formulas in Eq. (2) that x_d, y_d, and z_{max} also scale with α, while β and γ remain unchanged regardless the value of α. Recall this type of ambiguity was previously described as an infinite "family" of trajectories possessing the same line-of-sight history, whose (Cartesian) relative state values at any given time are scale multiples of one another. In terms of ROEs, we can say that this family of trajectories all possess the same β and γ history, while a_e, x_d, y_d, and z_{max} of these trajectories are related by scale multiples.

Obviously, actual relative motion between space objects is not linear. In reality, if one were to construct a "family" of relative orbits whose states at a particular time were all scale mutliples of one another (i.e. each orbit corresponding to a particular α), the relative orbits would have similar, but not identical, LOS histories. This is illustrated in Figure 3, whereby two relative orbits whose initial conditions are scale multiples of each other are propagated forward with nonlinear dynamics. It is seen that the LOS histories of the two trajectories are not identical, as would be predicted by linear dynamics, but in fact deviate increasingly over time. The members of this hypothetical family of relative orbits that are closer to the observer (where "closer" implies smaller values of the relative states) would have LOS histories closer to that predicted by linear dynamics, whereas the farther from the observer a particular family member is (i.e. the larger the relative orbit), the more its LOS history will deviate from the linear model. It is the authors' general contention that the amount of deviation, or dis-similarity, in a relative orbit compared to that predicted by linear dynamics is correlated with the degree of nonlinearity in the orbit, and correspondingly the degree of observability. That is, the closer a particular relative motion scenario is

to linear behavior (i.e. the less separation or difference between the observer and RSO orbits), the weaker the observability and the more difficult it is to determine the unique relative orbit (particularly its "size" or scale factor). Conversely, larger relative orbits will possess higher observability.

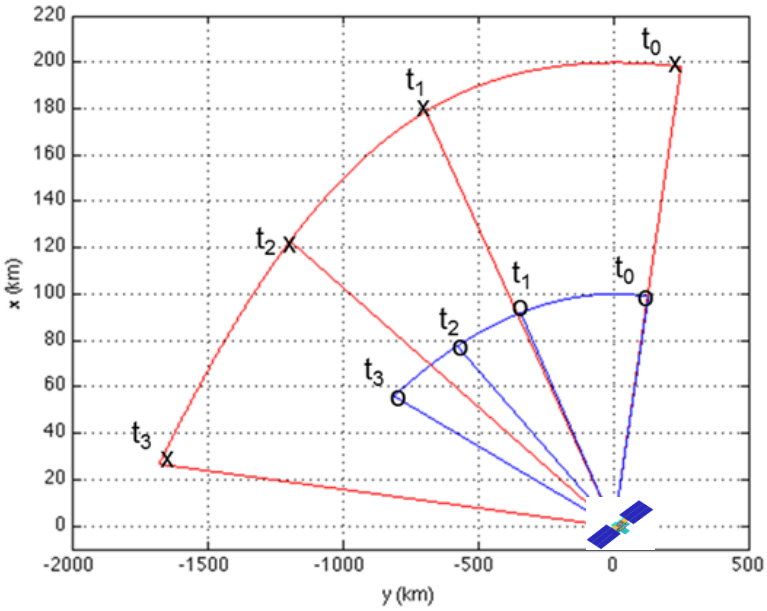

Figure 3. Illustration of observability afforded by nonlinearity: LOS histories of two relative orbits propagated forward with nonlinear dynamics.

Solving the Measurement Equations

We know that any IROD method resulting in a set of linear homogeneous measurement equations (i.e. of the form $A\bar{x}_0 = 0$) has no hope of determining the unique relative orbit, due to the infinite ambiguity discussed in the previous section. However, an IROD method based on a dynamic model that captures some degree of nonlinearity should have at least a possibility of success. The IROD method presented here utilizes the 2nd-order QV solution detailed above. Note that the *x*, *y*, and *z* components of this solution can each possess up to 27 terms. Thus, each expression is of the form

$$\begin{aligned} x(t) &= C_1(t)x_0 + C_2(t)y_0 + \ldots + C_6(t)\dot{z}_0 + C_7(t){x_0}^2 + C_8(t)x_0y_0 + \ldots + C_{27}(t){\dot{z}_0}^2 \\ y(t) &= D_1(t)x_0 + \ldots + D_{27}(t){\dot{z}_0}^2 \\ z(t) &= E_1(t)x_0 + \ldots + E_{27}(t){\dot{z}_0}^2 \end{aligned} \tag{9}$$

Evaluating *x(t)*, *y(t)*, and *z(t)* at measurement time t_i and inserting into Eq. (5) yields

$$\begin{aligned}
&\left[-u_z(t_i)D_1(t_i)+u_y(t_i)E_1(t_i)\right]x_0 + \ldots + \left[-u_z(t_i)D_{27}(t_i)+u_y(t_i)E_{27}(t_i)\right]\dot{z}_0{}^2 = 0\\
&\left[u_z(t_i)C_1(t_i)-u_x(t_i)E_1(t_i)\right]x_0 + \ldots + \left[u_z(t_i)C_{27}(t_i)-u_x(t_i)E_{27}(t_i)\right]\dot{z}_0{}^2 = 0\\
&\left[-u_y(t_i)C_1(t_i)+u_x(t_i)D_1(t_i)\right]x_0 + \ldots + \left[-u_y(t_i)C_{27}(t_i)+u_x(t_i)D_{27}(t_i)\right]\dot{z}_0{}^2 = 0
\end{aligned} \tag{10}$$

Note that each of these equations is a second-order polynomial in six unknowns (the six initial relative states). Following the procedure of the previous subsection, if we obtain three LOS measurements, choosing two of the measurement equations at each time, this yields a "square" system of six coupled second-order polynomials in the six initial relative states. Note that these equations are *not* linear in the initial relative states, i.e. they cannot be written as $A\bar{x}_0 = 0$. Thus, if $\bar{x}_0^*$ is a solution to these equations, $\alpha\bar{x}_0^*$ is not, i.e. we have escaped the infinite ambiguity of Woffinden's dilemma by employing nonlinear relative dynamics. The branch of applied mathematics known as numerical algebraic geometry offers multiple approaches to solving polynomial systems. In this paper, a method known as homotopy continuation is utilized, specifically, an algorithm derived and presented in Ref. 14.

Some discussion is in order regarding the number of solutions to the polynomial system. According to Bezout's Theorem,[15] there are a^b solutions to a system of coupled polynomials, where a represents the order of each polynomial and b represents the number of polynomials (i.e. number of variables). For six 2nd-order polynomials, the number of solutions is then 64. However, these solutions are in the complex domain, i.e. it is possible that each solution may consist of one or more values with imaginary parts. There is no known theorem for how many real solutions may exist, so the best that can be said is that the *maximum* number of real solutions for a given scenario is 64. If in fact multiple real solutions exist, we have a finite ambiguity to deal with (unlike the infinite ambiguity associated with Woffinden's dilemma). While the authors have devised a clear strategy for disambiguation of the solutions, this process will not be discussed here.

EXAMPLE CASES

In order to present and explain results as clearly as possible over numerous example cases, we first give a specific description and delineation of a simulated "case." We then describe the orbital scenarios included in the results, and the IOD and IROD methods to be utilized.

Definition of a "Case"

Following are the parameters and properties that fully define a case, along with a description specific to the analysis of this paper:

- **Initial conditions**: these are specified in terms of the observer and RSO orbit elements, as detailed below.
- **Propagation scheme**: this entails the orbit propagation method used to generate simulated measurements; for this analysis, both the observer & RSO orbits are propagated with two-body dynamics.
- **Measurement times**: the LOS measurement times are detailed below.

Initial Condition Scenarios

Two particular orbital scenarios are explored here, both of which are detailed in Table 1 in terms of the observer and RSO orbit elements at time $t_0 = 0$, including semimajor axis (a), eccentricity (e), inclination (i), right ascension of ascending node (Ω), argument of perigee (ω), and true anomaly (ν). The first scenario was defined in Reference 9 and is thus referred to as the "Williamsburg" scenario. This scenario does not pertain to a specific mission application, rather the conditions were chosen with some arbitrariness to effect several aspects of relative motion such as motion in all three dimensions and significant drift between the observer and RSO. This scenario is shown in Figure 4. The second scenario results in a 200 km x100 km ellipse in the LVLH *x*-*y* plane, with cross-track (*z*) motion of approximately 19 km amplitude. This scenario is referred to simply as the "200x100 Ellipse" scenario and is indicative of a rendezvous mission whereby one spacecraft is circumnavigating another in relative space. This scenario is shown in Figure 5.

Table 1. Scenario Initial Conditions

Scenario	Orbit	a (km)	e	i (deg)	Ω (deg)	ω (deg)	ν (deg)
Williamsburg	Observer	7.1000E+03	0.0000E+00	7.0000E+01	4.5000E+01	0.0000E+00	0.0000E+00
	RSO	7.1390E+03	5.4442E-03	7.0153E+01	4.5000E+01	3.5718E+02	2.8181E+00
200x100 Ellipse	Observer	7.1000E+03	0.0000E+00	7.0000E+01	4.5000E+01	0.0000E+00	0.0000E+00
	RSO	7.1000E+03	1.4085E-02	7.0155E+01	4.5000E+01	1.8000E+02	1.7999E+02

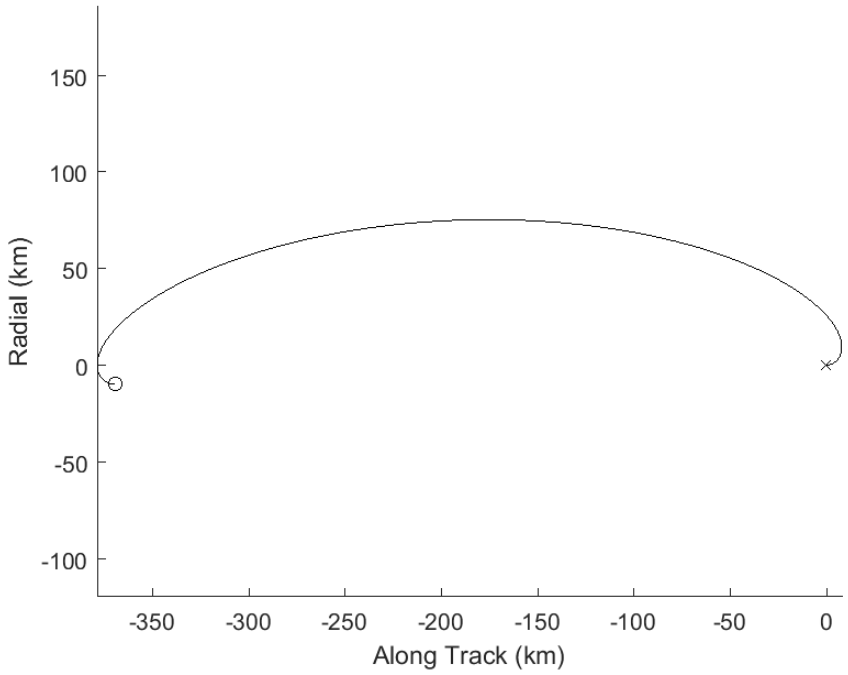

Figure 4: True Relative Orbit for "Williamsburg" Scenario.

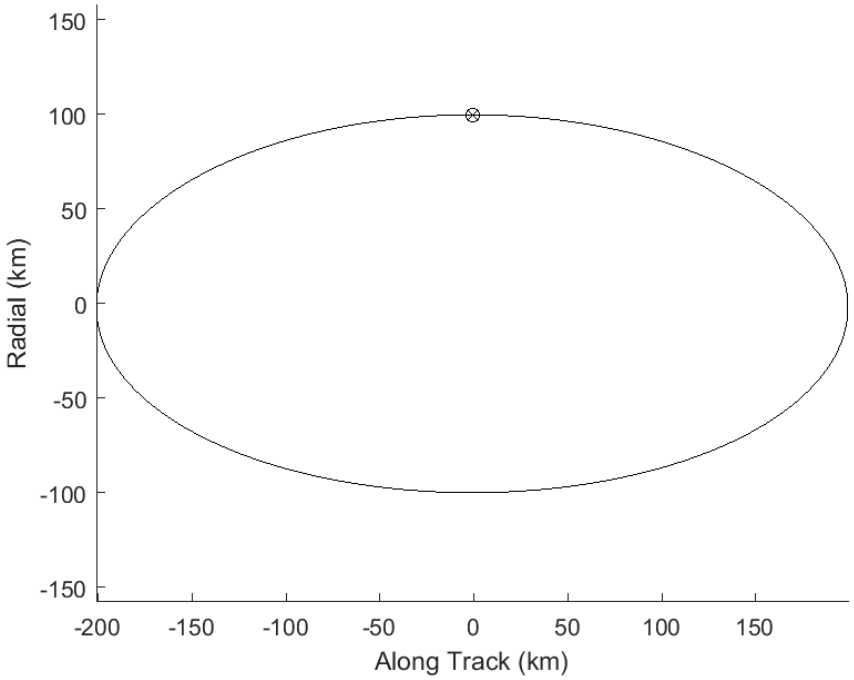

Figure 5: True Relative Orbit for "200x100 Ellipse" Scenario

Measurement Times

Table 2 displays the measurement times (t_1, t_2, t_3) chosen for the various cases. For the "Williamsburg" scenario, it was decided to hold t_2 constant at 2871.0844 sec (roughly ½ orbital period) and vary t_2 - t_1 (defined "Δt_1") and t_3 - t_2 (defined "Δt_3"). This resulted in six different sets of measurement times, comprising Cases I-VI in Table 2. Note that some choices of measurement times are symmetric ($\Delta t_1 = \Delta t_3$) while some are asymmetric ($\Delta t_1 \neq \Delta t_3$). For the "200x100 Ellipse" scenario, three sets of symmetric measurement times were chosen at various intervals within an orbital period, comprising Cases VII-IX in Table 2.

Table 2. Case Introduction (All Times in sec)

Case	Type	t2	Δt1	Δt3
I	Williamsburg	2871.0844	2	2
II	Williamsburg	2871.0844	30	30
III	Williamsburg	2871.0844	20	40
IV	Williamsburg	2871.0844	40	20
V	Williamsburg	2871.0844	100	100
VI	Williamsburg	2871.0844	300	300
VII	200X100 Ellipse	744.2327	50	50
VIII	200X100 Ellipse	1475.2346	50	50
IX	200X100 Ellipse	2219.4673	50	50

IOD/IROD Methods Implemented

The following methods were implemented in each of the above cases:

- Laplace's method to yield the inertial position and velocity vector of the RSO at t_2
- Gauss' method to yield the inertial position vector of the RSO at t_2, followed by Gibbs' method to obtain the inertial velocity vector at t_2
- Gauss' method to yield the inertial position vector of the RSO at t_2, followed by the Herrick-Gibbs method to obtain the inertial velocity vector at t_2
- Gauss' method to yield the inertial position vector of the RSO at t_2, followed by a method based on f and g series (with velocity terms truncated) to obtain the inertial velocity vector at t_2
- The IROD method described above, based on a 2nd-order model of relative dynamics, which yields the inertial position and velocity vector of the RSO at t_1

The Laplace and Gauss methods above are detailed in References 1-3. The inputs for these methods at each measurement time are the observer's position vector relative to Earth's center and the LOS vector, both expressed in an inertial frame, while the inputs for the IROD method are the observer's orbit radius and the LOS vector at each measurement time, expressed in the LVLH frame. All of these inputs can be generated from the information in Table 1 and Table 2.

PERFORMANCE METRICS

Here we describe the metrics that were calculated in order to gauge the performance of the various methods. They are LOS residual, orbit element ratios and differences, and ROE ratios and differences. Each metric involves a comparison between the true RSO orbit and the orbit calculated via IOD or IROD.

LOS Residual

This metric is calculated by propagating the IOD/IROD solution orbit forward to the three measurement times, computing the LOS based on the solution orbit (call this "estimated LOS") at each measurement time, computing the angle between the true LOS and estimated LOS at each measurement time, and computing the root-mean-square of these three angles. The formula for LOS residual is as follows:

$$LOS\ residual = \sqrt{\frac{\alpha_1^{\,2} + \alpha_2^{\,2} + \alpha_3^{\,2}}{3}} \quad where\ \alpha_i = \cos^{-1}\left(\hat{u}_{i,soln} \cdot \hat{u}_{i,measured}\right) \qquad (11)$$

This metric tells us how closely the solution orbit fits the three LOS constraints.

Orbit Element Ratios and Differences

These metrics are calculated by converting the IOD/IROD solution into the RSO orbit elements, then computing the ratio of estimated semimajor axis to true semimajor axis, and the differences between true and estimated eccentricity, true and estimated inclination, true and estimated right ascension of ascending node, and true and estimated argument of latitude. Obviously this metric tells us how closely the solution orbit matches the true RSO orbit.

ROE Ratios and Differences

ROEs were described above as a convenient way to characterize Clohessy-Wiltshire (i.e. linear) relative motion. Suppose for a moment that the relative motion between an observer and RSO behaved according to Clohessy-Wiltshire rather than real motion, and we wish to compare our estimated orbit to the true orbit. At any chosen time, we can calculate the ROE values for both

orbits. It was shown above that, within a family of trajectories, a_e, x_d, y_d, and z_{max} will scale up or down consistently. Thus, if our estimated orbit captures the proper "family" of the true trajectory but fails to capture the proper "α" scale factor, the ratio of the estimated value of a_e to the true value of a_e, the ratio of the estimated x_d to the true x_d, a the ratio of the estimated y_d to the true y_d, nd the ratio of the estimated z_{max} to the true z_{max} will all be equal. That is:

$$\frac{a_{e,est}}{a_{e,true}} = \frac{x_{d,est}}{x_{d,true}} = \frac{y_{d,est}}{y_{d,true}} = \frac{z_{\max,est}}{z_{\max,true}} \tag{12}$$

If in fact the estimate captures the proper scale factor α as well, these ratios will be 1. In the case of β and γ, because a family of trajectories at any given time will share the same values of these parameters (under Clohessy-Wiltshire assumptions) regardless the value of α, this means that if the estimate captures the proper "family" of the true trajectory, the value of β and γ for the estimate will match β and γ of the true trajectory, i.e., we have

$$\beta_{est} - \beta_{true} = \gamma_{est} - \gamma_{true} = 0 \tag{13}$$

In reality, relative motion does not precisely follow the Clohessy-Wiltshire model, although the closer proximity between observer and RSO, the more actual motion resembles Clohessy-Wiltshire. Therefore, in scenarios where the RSO is not prohibitively far from the observer, ROE ratios can be useful in assessing the quality of an IROD solution. That is, the equivalent of Eq. (12) would be

$$\frac{a_{e,est}}{a_{e,true}} \approx \frac{x_{d,est}}{x_{d,true}} \approx \frac{y_{d,est}}{y_{d,true}} \approx \frac{z_{\max,est}}{z_{\max,true}} \tag{14}$$

and the equivalent of Eq. (13) would be

$$\beta_{est} - \beta_{true} \approx \gamma_{est} - \gamma_{true} \approx 0 \tag{15}$$

RESULTS

The first portion of results involves the 9 example cases detailed in Table 1 and Table 2. For each of these cases, the 5 IOD/IROD methods above—Laplace, Gauss with 3 different to estimate velocity, and 2nd-order IROD—were executed. It should be noted that each method has the possibility to yield multiple solutions: Laplace and Gauss both involve an 8th-order polynomial in terms of the RSO's orbit radius at t_2, and the IROD method yields 64 solutions in the complex domain (as mentioned previously). Since disambiguation of solutions is not covered in this paper, for simplicity, each time a method yielded multiple solutions, the authors chose the solution closest to the true orbit. That is, for Laplace and Gauss the authors chose the root of the polynomial closest to the true RSO orbit radius at t_2, and for IROD the authors chose the solution whose LVLH states were closest to the true LVLH states.

Tables 3-11 display the error metrics detailed previously (LOS residual, orbit element ratios and differences, and ROE ratios and differences) for each method applied in each of the 9 example cases. LOS residual was calculated as in Eq. (11), and orbit element/ROE ratios and differ-

ences were calculated as described above. For Laplace and Gauss, because these methods are designed to yield a solution at t_2, all ratios and differences are calculated at t_2. For 2nd-order IROD, because this method is designed to yield a solution at t_1, all ratios and differences are calculated at t_1.

Before discussing these results in detail, several general statements can be made:

- For each IOD/IROD method, there is at least one case where the LOS residual is at or near 180°. In such a case, the method yields a trajectory whose LOS vector aligns closely with the true LOS vector at each measurement time, but in the opposite direction. Upon close study of each method, one can see that each method allows this possibility. In the case of 2nd-order IROD (the only method detailed in this paper), one can see from Eq. (4) that the LOS measurement at each measurement time (arising from the cross product of two vectors equaling zero) is satisfied whether $\bar{r}(t_i)$ points in the same direction as $\hat{u}_r(t_i)$ or the opposite direction.

- Both Laplace and 2nd-order IROD always include the trivial solution (whereby the RSO orbit is identical to the observer orbit) among the solution orbits yielded. With Laplace, this is indicated by one of the roots of the 8th-order polynomial being equal to the observer's orbit radius at t_2. With 2nd-order IROD, this is indicated by the fact that the polynomial measurement equations in Eq. (10) are homogeneous, thus the 6x1 zero vector is always a solution. For space-based observers this makes logical sense, because if the RSO's orbit were identical to that of the observer (if such a thing were possible), such an orbit would satisfy *any* given LOS measurement history. That is, for any given $\hat{u}_r(t_i)$, if the RSO were zero distance from the observer, $\hat{u}_r(t_i)$ would be guaranteed to point to the RSO. This phenomenon does not occur with Gauss, possibly because it would cause one of the matrices constructed as part of the method to be singular.

- For Laplace and Gauss, it should be mentioned that the only roots of the 8th-order polynomial representing a viable orbit solution are roots that are real, positive, and (in the case of Laplace) non-trivial. For Laplace, there is one of the 9 cases explored for which the method fails to yield a viable root (Case IV). Similarly, all three versions of Gauss fail to yield a viable solution in Case VIII.

The first thing to note about Tables 3-11 is the consistency of the LOS residual values across all cases and methods explored; namely, every LOS residual is very near zero or, in a few cases, 180°. This makes logical sense, as all the methods are designed to match the LOS constraints as closely as possible. Figures 6-14 display several propagated relative orbits in the *x*-*y* (radial/along-track) plane of the LVLH frame. For each case, the solution yielded by each method was propagated from t_0 with two-body dynamics for one orbit period of the observer, with "x" and "o" marking the start and end of each trajectory, respectively. Each plot also depicts the true LOS vector at each measurement time, as well as a "*" time tick along each trajectory at each measurement time.

A brief assessment of each method's performance in these cases is now given:

- Laplace performs extremely well in Cases I and IX, as evidenced by both the ROE ratios and trajectory plots. In both cases, Laplace produces the best solution of all the methods, and there is very little difference between its propagated relative orbit and the true relative orbit. In Cases II and VII, the Laplace solution is fairly accurate, suf-

fering only from a "scale factor error" whereby the size of the relative orbit is slightly larger or smaller than the true relative orbit. In Cases III and VI, the Laplace solution suffers from the 180° LOS residual discussed above, and in Case IV Laplace fails to find a viable orbit solution (also mentioned above).

- All three versions of Gauss generally perform very poorly in this analysis. In fact, Figures 6-14 display each case with and without the Gauss relative orbits because they tend to be so much larger in magnitude than the other trajectories. In fact, the only cases where Gauss produces a remotely acceptable results are Cases VII and IX.
- 2nd-order IROD is clearly the most consistent performer. It never seems to under- or over-shoot the magnitude of the true relative orbit by very much except in Case VII where the IROD relative orbit can barely be seen (and is also 180° out of phase).

Table 3. Case I Error Metrics (All Residuals and Differences in deg)

	Semimajor Axis Ratio	Eccentricity Difference	Inclination Difference	Ω Difference	Arg. Of Lat. Difference	Line of Sight Residual
Lapace	1.0000E+00	-6.4277E-07	-2.0570E-05	5.6665E-07	1.8552E-04	6.9710E-07
Gauss: Gibbs	9.9076E-01	2.4980E-02	-6.6486E-01	-6.9020E-02	6.5561E+00	1.8000E+02
Herrick-Gibbs	9.9073E-01	2.4947E-02	-6.6486E-01	-6.9020E-02	6.5561E+00	1.8000E+02
F and G Series	9.9073E-01	2.4947E-02	-6.6486E-01	-6.9020E-02	6.5561E+00	1.8000E+02
Second Order	9.9902E-01	-7.4058E-04	-2.3718E-02	5.6584E-04	2.1337E-01	4.9293E-07
	a_e Ratio	x_d Ratio	y_d Ratio	z_max Ratio	β Difference	γ Difference
Lapace	9.9986E-01	9.9987E-01	9.9986E-01	9.9987E-01	1.0161E-04	-9.5907E-05
Gauss: Gibbs	2.9100E+00	-4.4659E+00	-3.4722E+00	3.4668E+00	-1.7866E+02	-1.4337E+00
Herrick-Gibbs	2.9037E+00	-4.4760E+00	-3.4721E+00	3.4665E+00	-1.7865E+02	-1.4413E+00
F and G Series	2.9037E+00	-4.4760E+00	-3.4721E+00	3.4665E+00	-1.7865E+02	-1.4413E+00
Second Order	8.3780E-01	8.5781E-01	8.4496E-01	8.4429E-01	-1.0829E-01	-2.3294E-02

Table 4. Case II Error Metrics (All Residuals and Differences in deg)

	Semimajor Axis Ratio	Eccentricity Difference	Inclination Difference	Ω Difference	Arg. Of Lat. Difference	Line of Sight Residual
Lapace	9.9973E-01	-2.0343E-04	-6.4732E-03	1.7076E-04	5.7081E-02	1.4037E-04
Gauss: Gibbs	1.0701E+00	1.4851E-02	8.7345E-01	-1.5177E-01	-7.1468E+00	7.2903E-04
Herrick-Gibbs	1.0698E+00	1.4943E-02	8.7345E-01	-1.5177E-01	-7.1468E+00	3.1497E-05
F and G Series	1.0698E+00	1.4950E-02	8.7345E-01	-1.5177E-01	-7.1468E+00	6.3446E-05
Second Order	9.9902E-01	-7.4097E-04	-2.3734E-02	5.6619E-04	2.0863E-01	5.6890E-05
	a_e Ratio	x_d Ratio	y_d Ratio	z_max Ratio	β Difference	γ Difference
Lapace	9.5736E-01	9.5806E-01	9.5742E-01	9.5787E-01	2.7603E-02	-2.5814E-02
Gauss: Gibbs	1.0630E+01	5.2107E-02	6.5607E+00	7.2484E+00	-9.9317E-03	7.6514E-01
Herrick-Gibbs	1.0663E+01	4.1007E-04	6.5583E+00	7.2437E+00	1.4812E-02	7.3576E-01
F and G Series	1.0663E+01	-2.1715E-04	6.5589E+00	7.2437E+00	8.1128E-03	7.4246E-01
Second Order	8.3260E-01	8.6580E-01	8.3726E-01	8.4423E-01	-1.6281E+00	-1.8464E-01

Table 5. Case III Error Metrics (All Residuals and Differences in deg)

	Semimajor Axis Ratio	Eccentricity Difference	Inclination Difference	Ω Difference	Arg. Of Lat. Difference	Line of Sight Residual
Lapace	9.9262E-01	-2.4777E-03	-2.2254E-01	-2.9521E-03	2.0244E+00	1.8000E+02
Gauss: Gibbs	1.0687E+00	1.4393E-02	8.6091E-01	-1.4791E-01	-7.0526E+00	6.6980E-05
Herrick-Gibbs	1.0687E+00	1.4384E-02	8.6091E-01	-1.4791E-01	-7.0526E+00	4.1241E-06
F and G Series	1.0687E+00	1.4394E-02	8.6091E-01	-1.4791E-01	-7.0526E+00	8.2181E-05
Second Order	9.9904E-01	-7.1896E-04	-2.3092E-02	5.5363E-04	2.0466E-01	5.7041E-05
	a_e Ratio	x_d Ratio	y_d Ratio	z_max Ratio	β Difference	γ Difference
Lapace	4.5107E-01	-4.8294E-01	-4.6293E-01	4.6468E-01	-1.7966E+02	-3.3034E-01
Gauss: Gibbs	1.0405E+01	2.0607E-01	6.4712E+00	7.1464E+00	9.7504E-02	6.4308E-01
Herrick-Gibbs	1.0402E+01	2.1072E-01	6.4714E+00	7.1469E+00	9.5301E-02	6.4570E-01
F and G Series	1.0403E+01	2.0986E-01	6.4724E+00	7.1468E+00	8.5421E-02	6.5558E-01
Second Order	8.3894E-01	8.6658E-01	8.4416E-01	8.4843E-01	-1.0860E+00	-1.2603E-01

Table 6. Case IV Error Metrics (All Residuals and Differences in deg)

	Semimajor Axis Ratio	Eccentricity Difference	Inclination Difference	Ω Difference	Arg. Of Lat. Difference	Line of Sight Residual
Lapace	N/A	N/A	N/A	N/A	N/A	N/A
Gauss: Gibbs	1.0705E+00	1.5081E-02	8.7718E-01	-1.5292E-01	-7.1747E+00	1.6497E-03
Herrick-Gibbs	1.0698E+00	1.5275E-02	8.7718E-01	-1.5292E-01	-7.1747E+00	8.8999E-05
F and G Series	1.0698E+00	1.5277E-02	8.7718E-01	-1.5292E-01	-7.1747E+00	1.0451E-04
Second Order	9.9899E-01	-7.6469E-04	-2.4427E-02	5.7956E-04	2.1295E-01	5.8737E-05
	a_e Ratio	x_d Ratio	y_d Ratio	z_max Ratio	β Difference	γ Difference
Lapace	N/A	N/A	N/A	N/A	N/A	N/A
Gauss: Gibbs	1.0704E+01	-5.5022E-03	6.5947E+00	7.2784E+00	-1.1704E-01	8.7635E-01
Herrick-Gibbs	1.0772E+01	-1.1348E-01	6.5896E+00	7.2686E+00	-6.4728E-02	8.1433E-01
F and G Series	1.0772E+01	-1.1370E-01	6.5898E+00	7.2686E+00	-6.6917E-02	8.1652E-01
Second Order	8.2595E-01	8.6463E-01	8.3006E-01	8.3971E-01	-2.1728E+00	-2.4062E-01

Table 7. Case V Error Metrics (All Residuals and Differences in deg)

	Semimajor Axis Ratio	Eccentricity Difference	Inclination Difference	Ω Difference	Arg. Of Lat. Difference	Line of Sight Residual
Lapace	9.9739E-01	-2.1961E-03	-6.6227E-02	1.0355E-03	3.4329E+01	5.2050E-03
Gauss: Gibbs	1.1035E+00	2.3919E-02	1.1025E+00	-2.3036E-01	-8.8351E+00	2.2049E-02
Herrick-Gibbs	1.0997E+00	2.3424E-02	1.1025E+00	-2.3036E-01	-8.8351E+00	2.8178E-03
F and G Series	1.0997E+00	2.3543E-02	1.1025E+00	-2.3036E-01	-8.8351E+00	3.9708E-03
Second Order	9.9901E-01	-7.4482E-04	-2.3855E-02	5.6887E-04	1.9748E-01	5.5797E-04
	a_e Ratio	x_d Ratio	y_d Ratio	z_max Ratio	β Difference	γ Difference
Lapace	5.6867E-01	5.6326E-01	5.6534E-01	5.6759E-01	2.1363E-01	-1.9622E-01
Gauss: Gibbs	1.4938E+01	-3.0693E+00	8.0451E+00	9.2811E+00	-2.6275E-01	1.3518E+00
Herrick-Gibbs	1.5228E+01	-3.5325E+00	8.0128E+00	9.2179E+00	-2.8245E-02	1.0705E+00
F and G Series	1.5236E+01	-3.5443E+00	8.0234E+00	9.2180E+00	-1.0278E-01	1.1451E+00
Second Order	8.1929E-01	8.8454E-01	8.1754E-01	8.4361E-01	-5.5011E+00	-5.1350E-01

Table 8. Case VI Error Metrics (All Residuals and Differences in deg)

	Semimajor Axis Ratio	Eccentricity Difference	Inclination Difference	Ω Difference	Arg. Of Lat. Difference	Line of Sight Residual
Lapace	9.8954E-01	6.6687E-03	-4.0719E-01	-1.9018E-02	2.8858E+00	1.7988E+02
Gauss: Gibbs	1.2248E+00	7.9106E-02	1.6312E+00	-4.6702E-01	-1.2425E+01	4.1629E-01
Herrick-Gibbs	1.1905E+00	6.1820E-02	1.6312E+00	-4.6702E-01	-1.2425E+01	1.2545E-01
F and G Series	1.1912E+00	6.3605E-02	1.6312E+00	-4.6702E-01	-1.2425E+01	1.8462E-01
Second Order	9.9900E-01	-7.5914E-04	-2.4263E-02	5.7927E-04	1.6607E-01	3.4467E-03
	a_e Ratio	x_d Ratio	y_d Ratio	z_max Ratio	β Difference	γ Difference
Lapace	1.8971E+00	-1.4110E+00	-1.6733E+00	1.6977E+00	-1.7823E+02	-1.7302E+00
Gauss: Gibbs	3.0315E+01	-1.9020E+01	1.1920E+01	1.5641E+01	-2.1484E+00	4.3407E+00
Herrick-Gibbs	3.1425E+01	-2.0825E+01	1.1517E+01	1.4806E+01	-6.8632E-01	2.5569E+00
F and G Series	3.1608E+01	-2.1107E+01	1.1695E+01	1.4818E+01	-1.2882E+00	3.1637E+00
Second Order	7.8415E-01	9.3158E-01	7.6130E-01	8.4169E-01	-1.7100E+01	-9.0932E-01

Table 9. Case VII Error Metrics (All Residuals and Differences in deg)

	Semimajor Axis Ratio	Eccentricity Difference	Inclination Difference	Ω Difference	Arg. Of Lat. Difference	Line of Sight Residual
Lapace	1.0001E+00	3.6002E-03	4.0945E-02	-1.0286E-04	-2.7621E-01	2.5289E-03
Gauss: Gibbs	1.0053E+00	3.8124E-02	4.8347E-01	-9.7750E-03	-3.3162E+00	6.5828E-03
Herrick-Gibbs	1.0044E+00	3.8843E-02	4.8347E-01	-9.7750E-03	-3.3162E+00	5.9063E-04
F and G Series	1.0044E+00	3.8871E-02	4.8347E-01	-9.7750E-03	-3.3162E+00	1.1034E-03
Second Order	1.0000E+00	-1.3488E-02	-1.6137E-01	-3.4616E-05	1.1158E+00	1.8000E+02
	a_e Ratio	x_d Ratio	y_d Ratio	z_max Ratio	β Difference	γ Difference
Lapace	1.2629E+00	1.2587E+00	1.4353E+00	1.2622E+00	7.1157E-02	-1.0497E-01
Gauss: Gibbs	4.0928E+00	5.0988E+00	5.6753E+00	4.0772E+00	-8.1988E-02	-1.8298E-01
Herrick-Gibbs	4.1287E+00	7.0155E+00	5.4604E+00	4.0732E+00	-6.2447E-01	4.1535E-01
F and G Series	4.1305E+00	7.0005E+00	5.6945E+00	4.0731E+00	-5.9133E-01	3.8321E-01
Second Order	4.1317E-02	-4.1375E-02	-3.7624E-02	4.1317E-02	1.7700E+02	2.8399E-03

Table 10. Case VIII Error Metrics (All Residuals and Differences in deg)

	Semimajor Axis Ratio	Eccentricity Difference	Inclination Difference	Ω Difference	Arg. Of Lat. Difference	Line of Sight Residual
Lapace	9.9814E-01	1.0837E-02	1.1831E-01	6.2504E-03	-1.2210E+00	9.5888E-04
Gauss: Gibbs	N/A	N/A	N/A	N/A	N/A	N/A
Herrick-Gibbs	N/A	N/A	N/A	N/A	N/A	N/A
F and G Series	N/A	N/A	N/A	N/A	N/A	N/A
Second Order	1.0000E+00	-3.6034E-05	-3.9972E-04	5.2411E-06	4.1542E-03	2.5551E-05
	a_e Ratio	x_d Ratio	y_d Ratio	z_max Ratio	β Difference	γ Difference
Lapace	1.7973E+00	4.9571E+00	3.8938E+00	1.7628E+00	-7.1537E+00	5.3167E+00
Gauss: Gibbs	N/A	N/A	N/A	N/A	N/A	N/A
Herrick-Gibbs	N/A	N/A	N/A	N/A	N/A	N/A
F and G Series	N/A	N/A	N/A	N/A	N/A	N/A
Second Order	1.0018E+00	9.9052E-01	3.0573E-01	9.9741E-01	-2.9295E+00	-4.5346E-02

Table 11. Case IX Error Metrics (All Residuals and Differences in deg)

	Semimajor Axis Ratio	Eccentricity Difference	Inclination Difference	Ω Difference	Arg. Of Lat. Difference	Line of Sight Residual
Lapace	1.0000E+00	5.1670E-04	5.3117E-03	-1.7949E-04	-4.1812E-02	2.5711E-03
Gauss: Gibbs	1.0075E+00	3.1616E-02	-7.4613E-01	-1.5024E-02	5.3692E+00	1.7999E+02
Herrick-Gibbs	1.0067E+00	3.2169E-02	-7.4613E-01	-1.5024E-02	5.3692E+00	1.8000E+02
F and G Series	1.0067E+00	3.2227E-02	-7.4613E-01	-1.5024E-02	5.3692E+00	1.8000E+02
Second Order	1.0026E+00	2.9782E-02	2.9969E-01	-4.9805E-03	-2.4854E+00	2.5195E-03
	a_e Ratio	x_d Ratio	y_d Ratio	z_max Ratio	β Difference	γ Difference
Lapace	1.0358E+00	9.9426E-01	9.4782E-01	1.0344E+00	-5.0633E-03	5.3912E-02
Gauss: Gibbs	3.8165E+00	-8.4855E-01	-2.5389E+00	3.7613E+00	-1.7925E+02	-3.3770E-01
Herrick-Gibbs	3.8469E+00	5.6516E-01	-2.6346E+00	3.7585E+00	-1.7875E+02	-8.8063E-01
F and G Series	3.8508E+00	5.3308E-01	-2.3057E+00	3.7583E+00	-1.7883E+02	-8.0285E-01
Second Order	2.9687E+00	3.4624E+00	2.0680E+00	2.9603E+00	-3.5056E+00	4.5167E-01

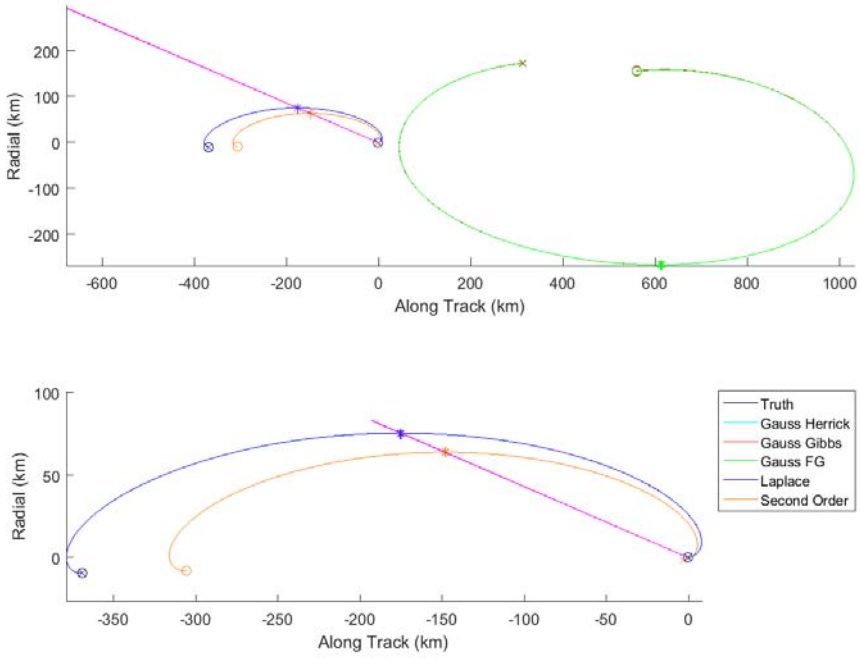

Figure 6: Case I Propagated Relative Orbits

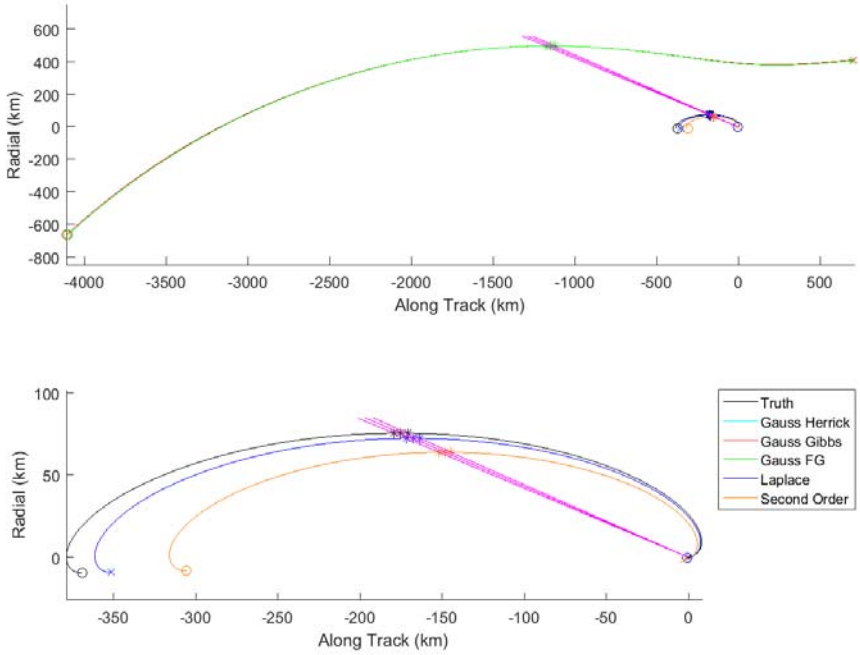

Figure 7: Case II Propagated Relative Orbits

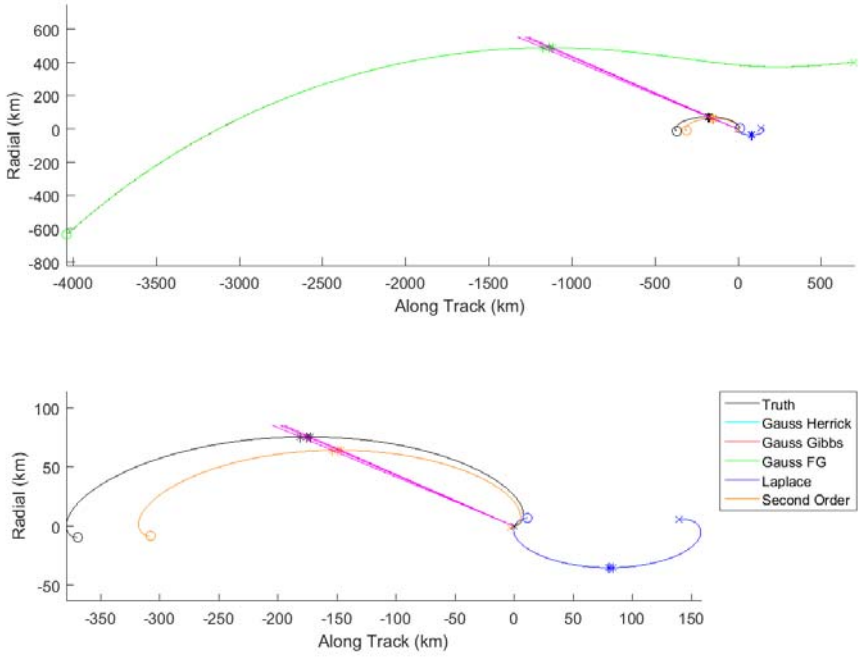

Figure 8: Case III Propagated Relative Orbits

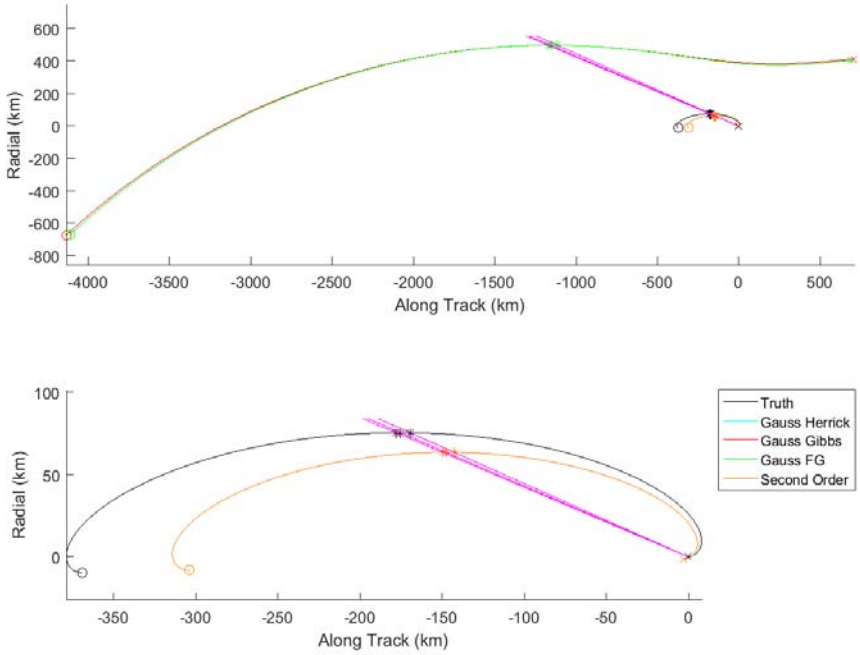

Figure 9: Case IV Propagated Relative Orbits

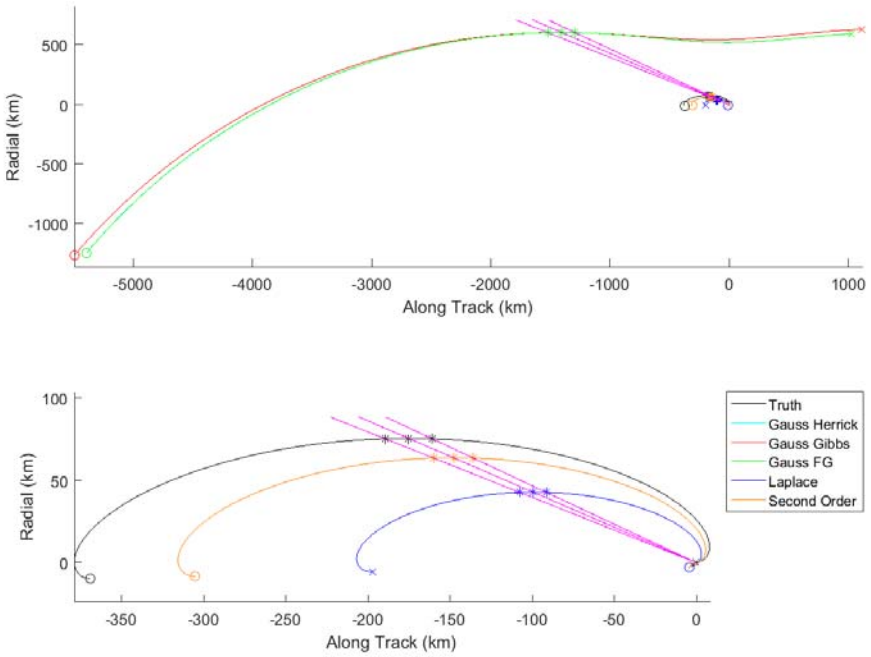

Figure 10: Case V Propagated Relative Orbits

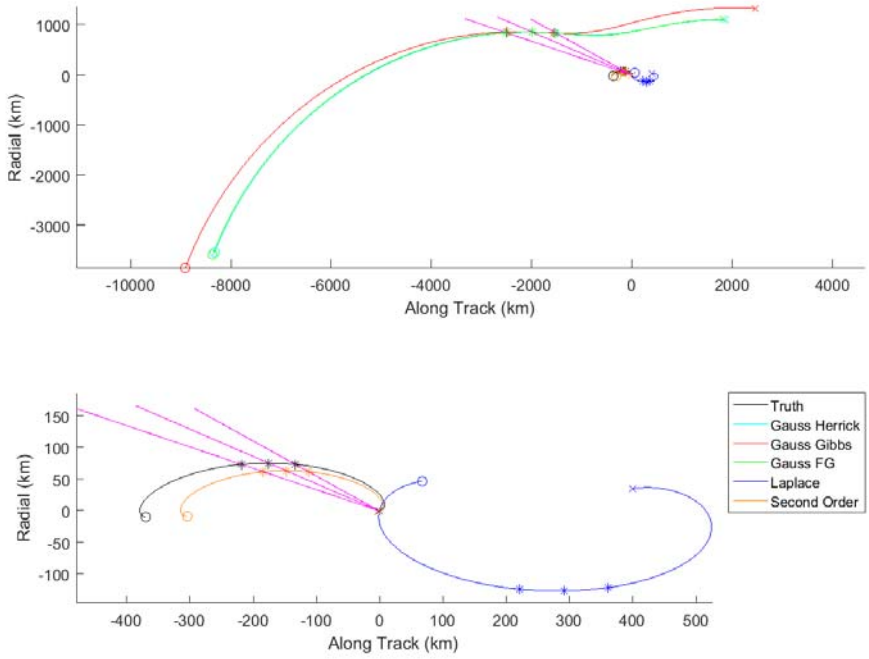

Figure 11: Case VI Propagated Relative Orbits

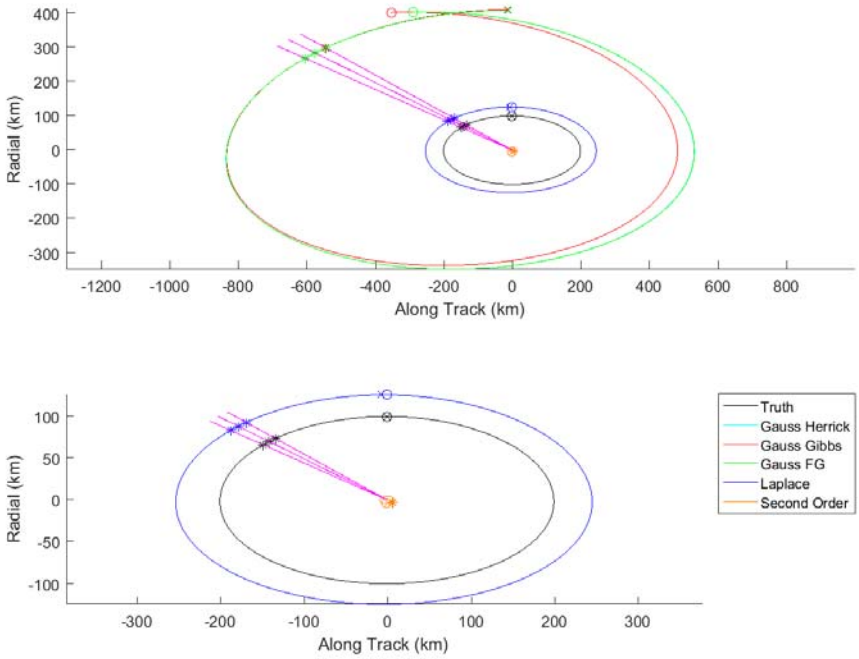

Figure 12: Case VII Propagated Relative Orbits

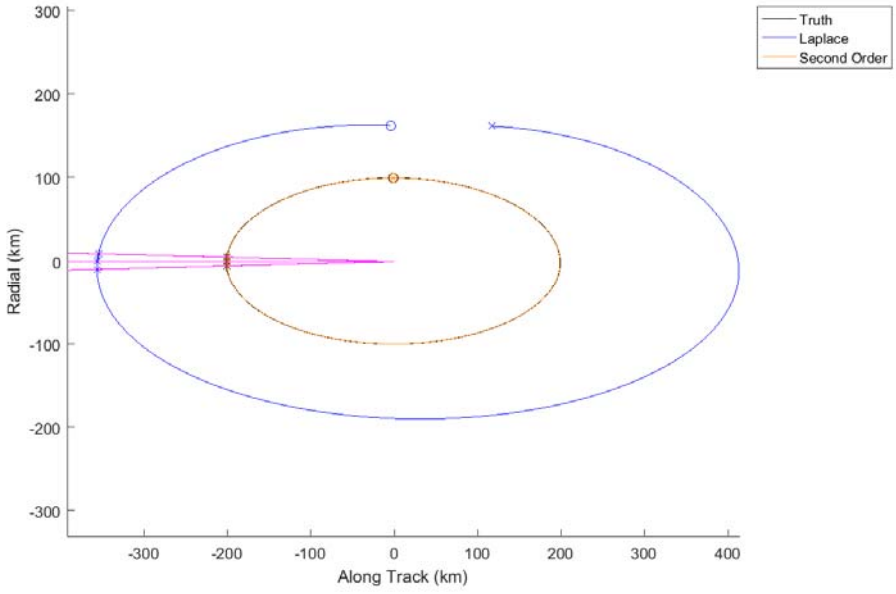

Figure 13: Case VIII Propagated Relative Orbits

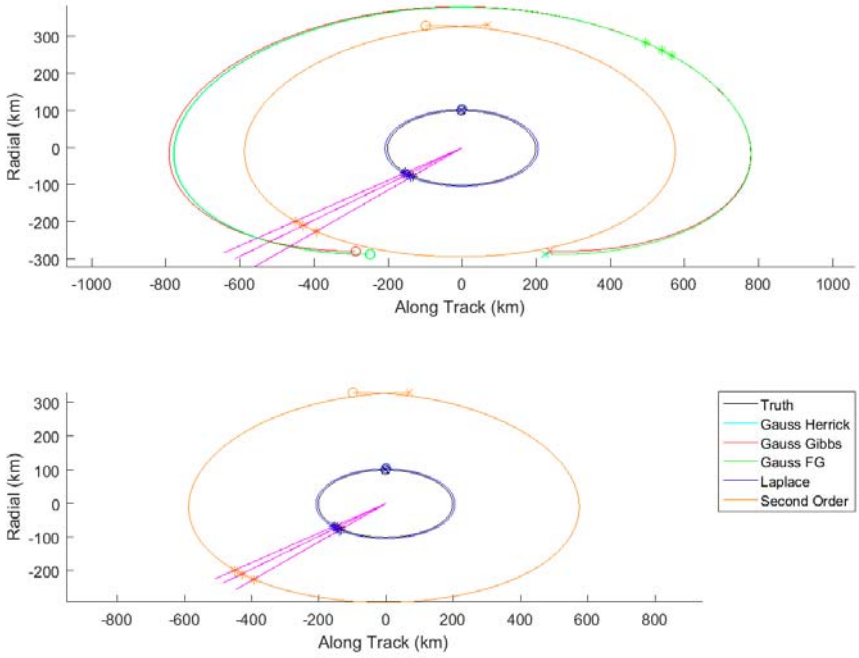

Figure 14: Case IX Propagated Relative Orbits

Since the accuracy of these methods appears to depend somewhat on the choice of measurement times, the methods were again applied to the "Williamsburg" and "200x100 Ellipse" scenarios over a wide range of measurement times. Referring back to Table 2, for the "Williamsburg" scenario the value of t_2 was the same as that in Cases I-VI (2871.0844 sec), while for the "200x100 Ellipse" scenario the value of t_2 was the same as that in Case IX (2219.4673 sec). The values of Δt_1 and Δt_3 were then allowed to vary from 0 (actually a value very near 0) to 1500 sec. The resulting contour and surface plots are in Figures 15-44.

A brief assessment of each method's performance based on these plots is now given:

- Laplace displays possibly the greatest dependence on choice of measurement times of all the methods. For both scenarios, the plots clearly contain a significant region where Laplace fails to find a viable orbit solution. In fact, the only region where Laplace seems to perform acceptably is near the boundary of this region: for the "Williamsburg" scenario this region is a thin arc stretching from around (0,0) to around (1500,750 sec). Outside this region, all the other values for which Laplace finds a viable orbit solution seem to also possess 180° LOS residual. For the "200x100 Ellipse" scenario, the region of acceptability seems slightly larger, also near the boundary of the no-solution region.
- While all three versions of Gauss seem to have a larger region of acceptable LOS residuals than Laplace, clearly their performance in terms of orbit element and ROE ratios and differences is generally poor except at very small Δt values.

- 2nd-order IROD appears to possess the least dependence on choice of measurement times of all the methods. Furthermore its accuracy across both scenarios seems quite good, except for a few areas for the "Williamsburg" scenario where its relative orbit is 180° out of phase.

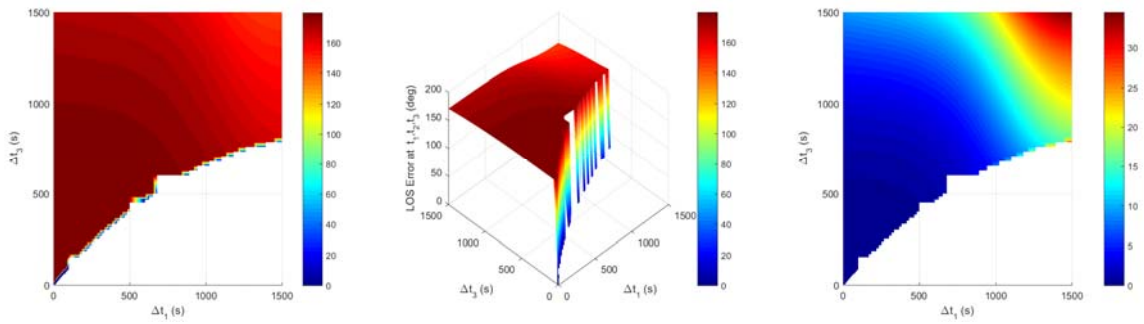

Figure 15. Laplace Line-of-Sight Residuals (deg), Williamsburg Scenario

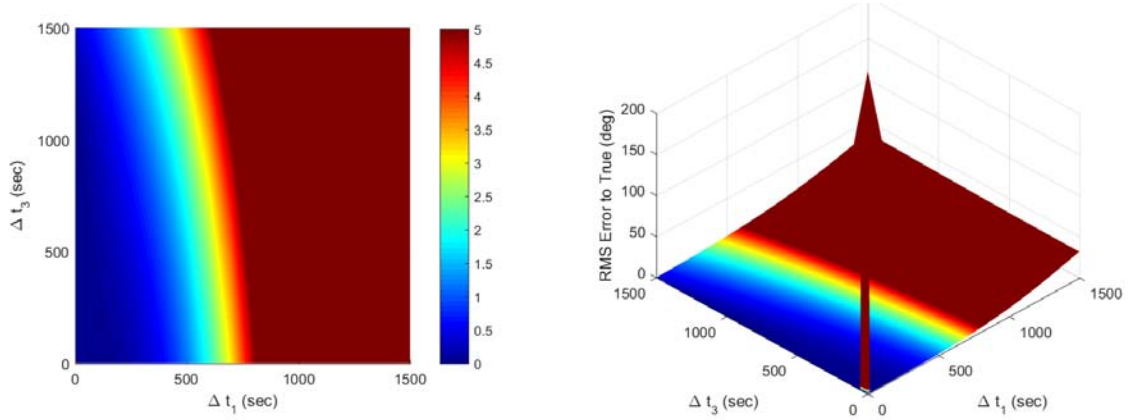

Figure 16. Gauss with Gibbs Velocity Line-of-Sight Residuals (deg), Williamsburg Scenario

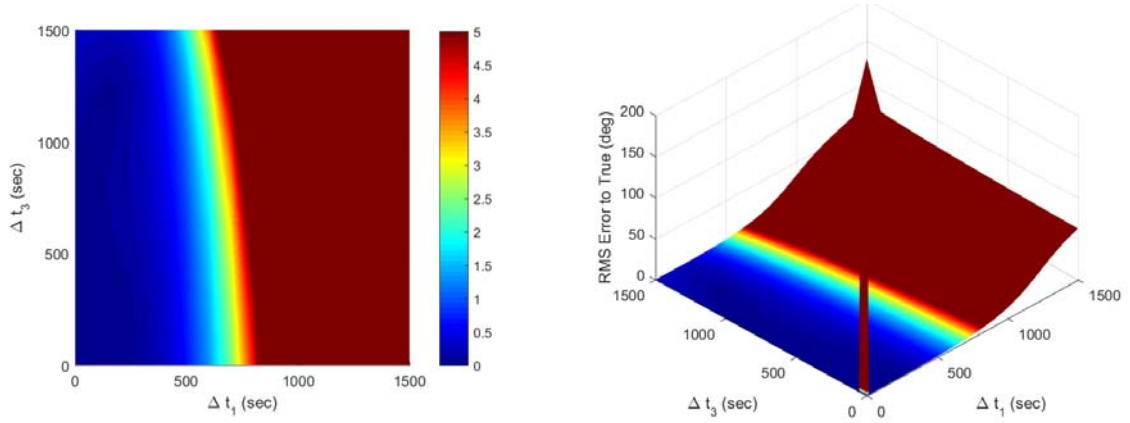

Figure 17. Gauss with Herrick Gibbs Velocity Line-of-Sight Residuals (deg), Williamsburg Scenario

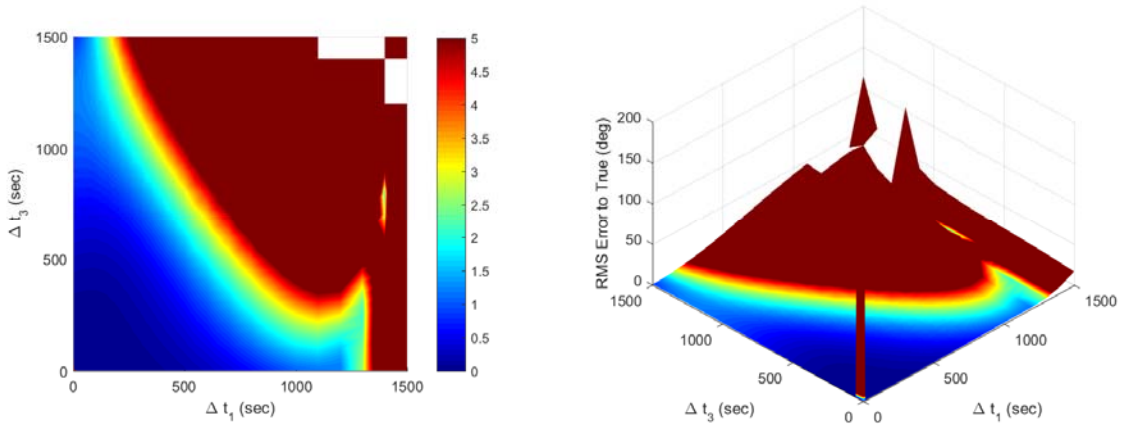

Figure 18. Gauss with Truncated F and G Series Velocity Line-of-Sight Residuals (deg), Williamsburg Scenario

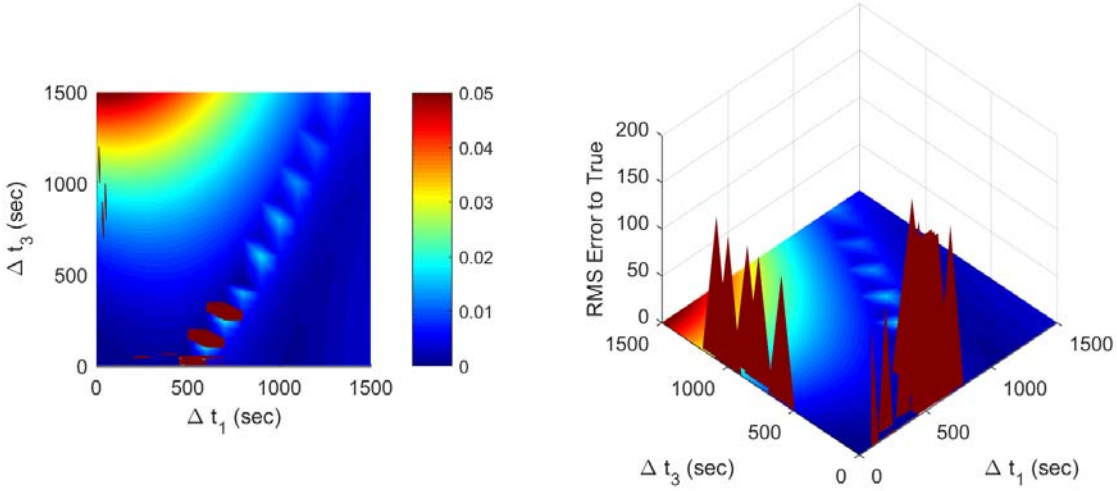

Figure 19. Second Order Line-of-Sight Residuals (deg), Williamsburg Scenario

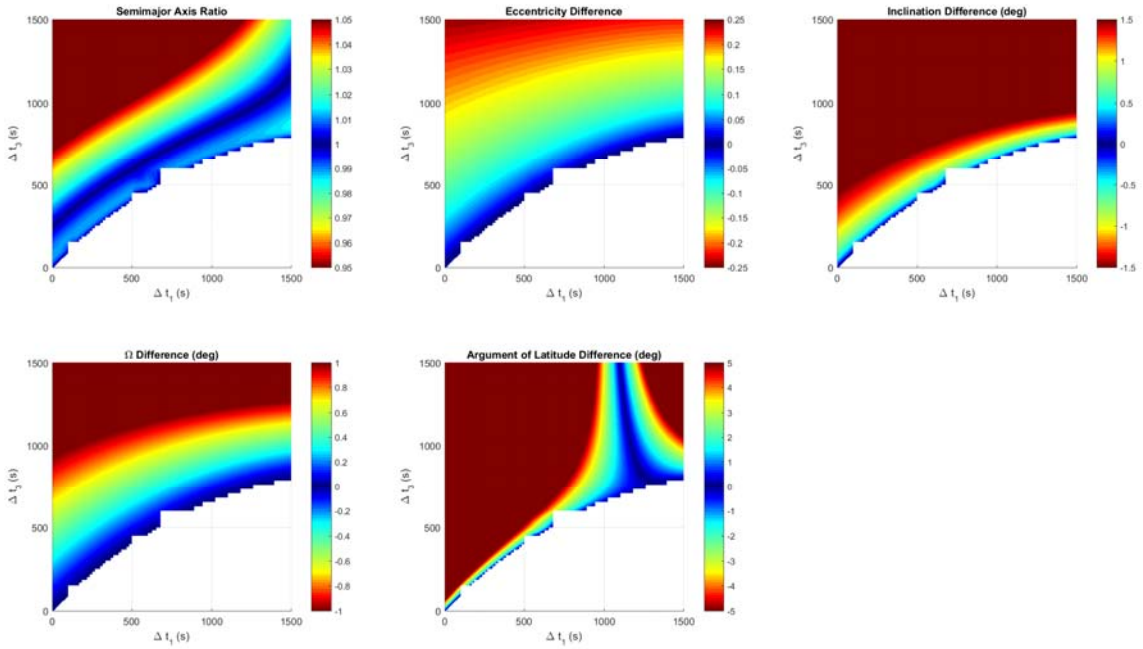

Figure 20. Laplace Orbital Element Ratios and Differences, Williamsburg Scenario

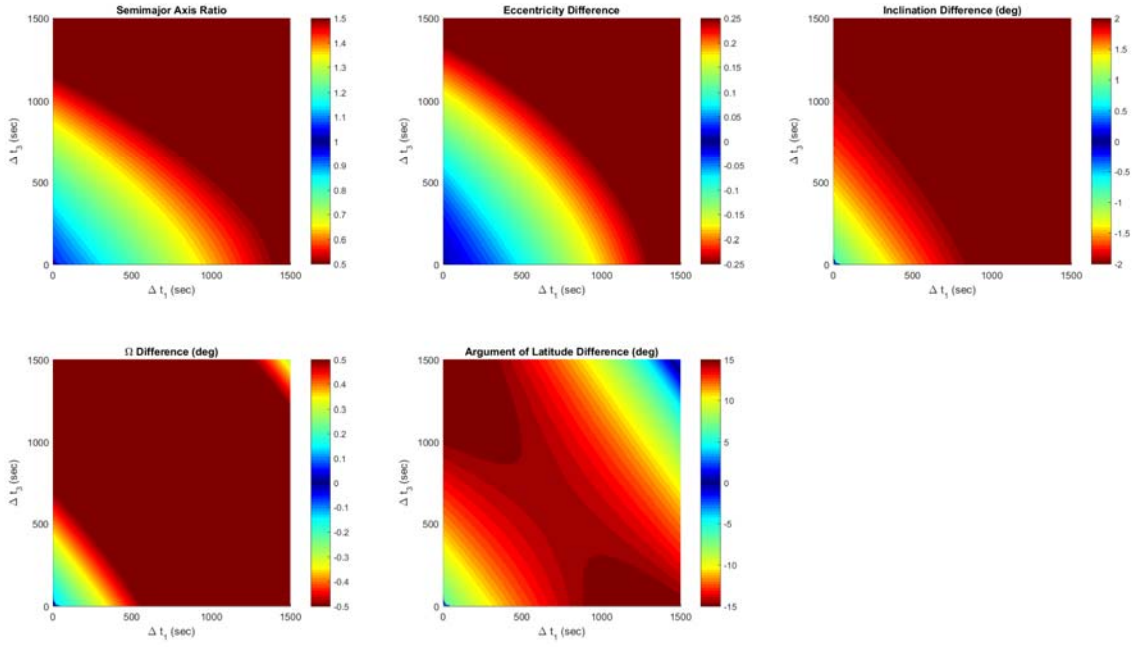

Figure 21. Gauss with Gibbs Velocity Orbital Element Ratios and Differences, Williamsburg Scenario

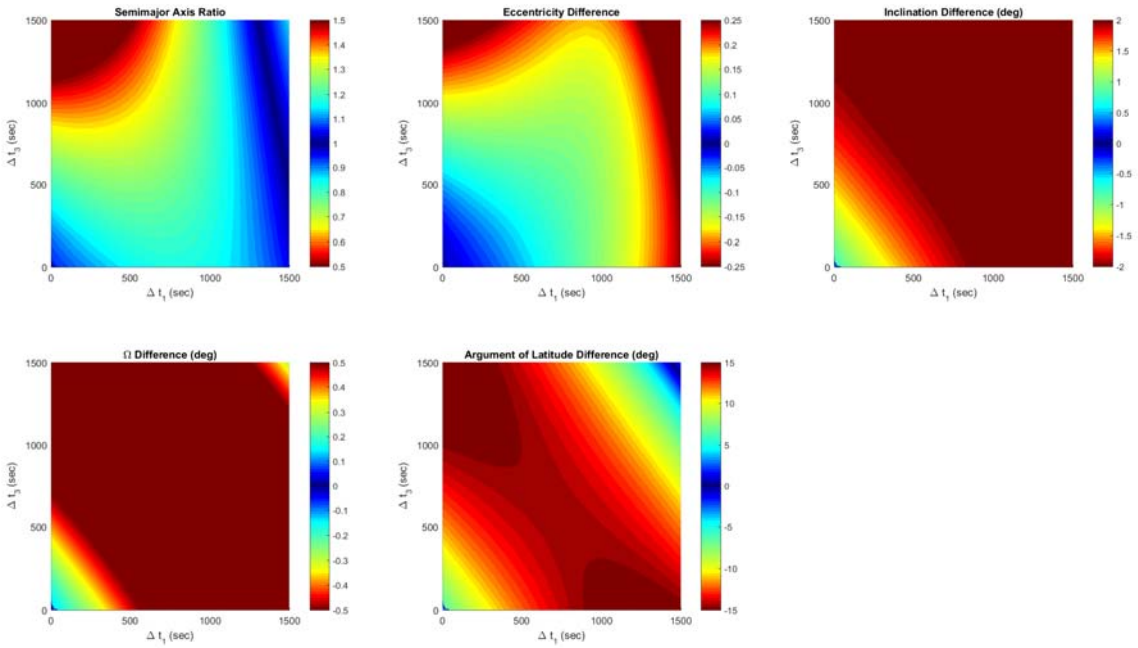

Figure 22. Gauss with Herrick Gibbs Velocity Orbital Element Ratios and Differences, Williamsburg Scenario

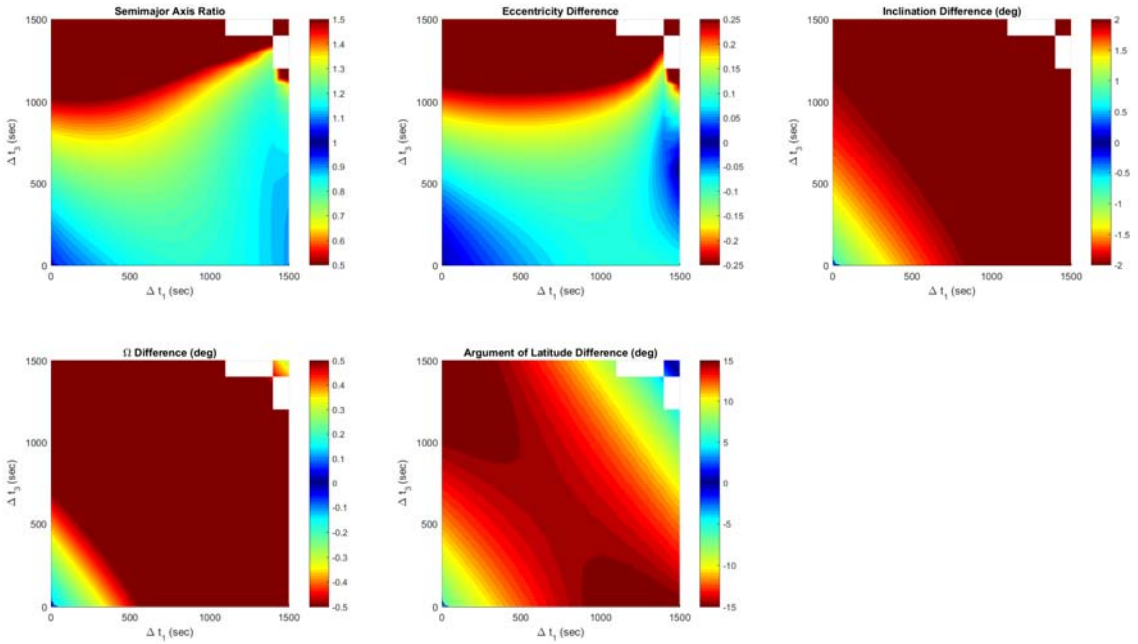

Figure 23. Gauss with Truncated F and G Series Velocity Orbital Element Ratios and Differences, Williamsburg Scenario

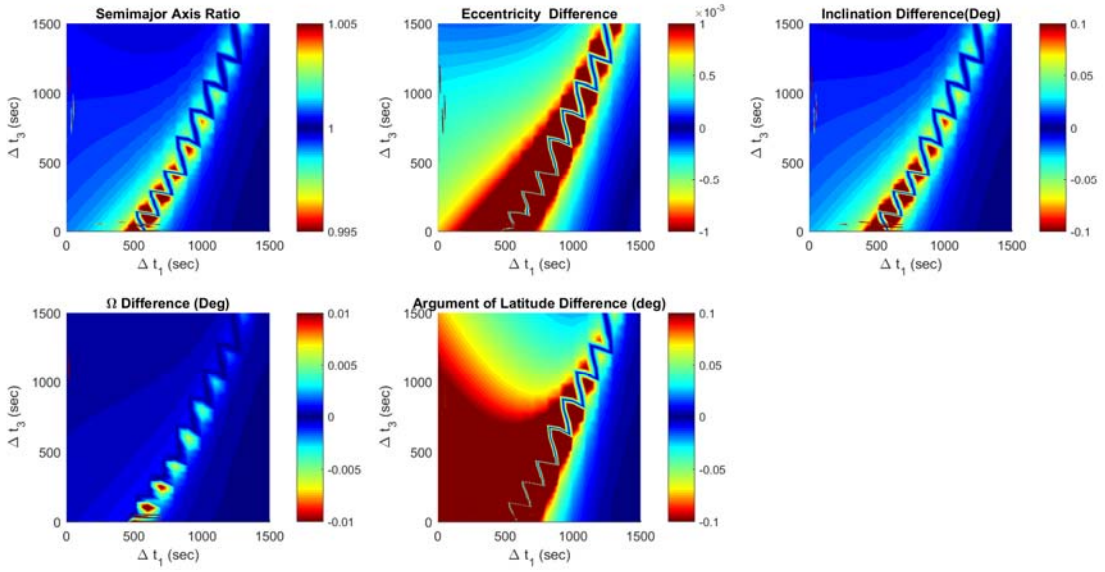

Figure 24. Second Order Orbital Element Ratios and Differences, Williamsburg Scenario

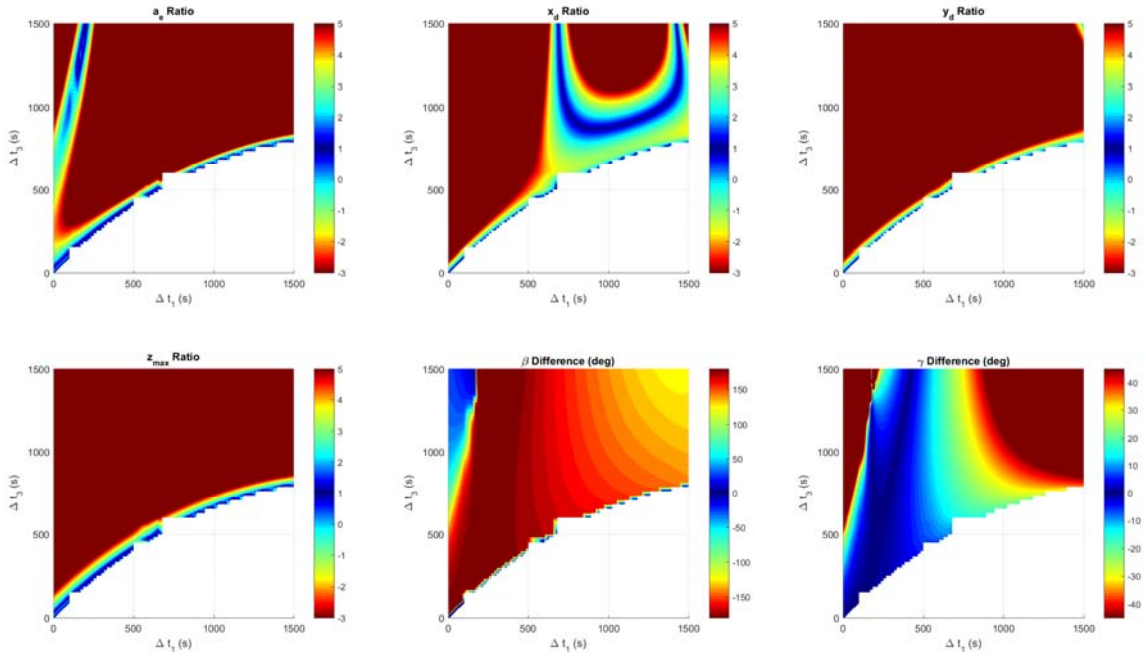

Figure 25. Laplace Relative Orbital Element Ratios and Differences, Williamsburg Scenario

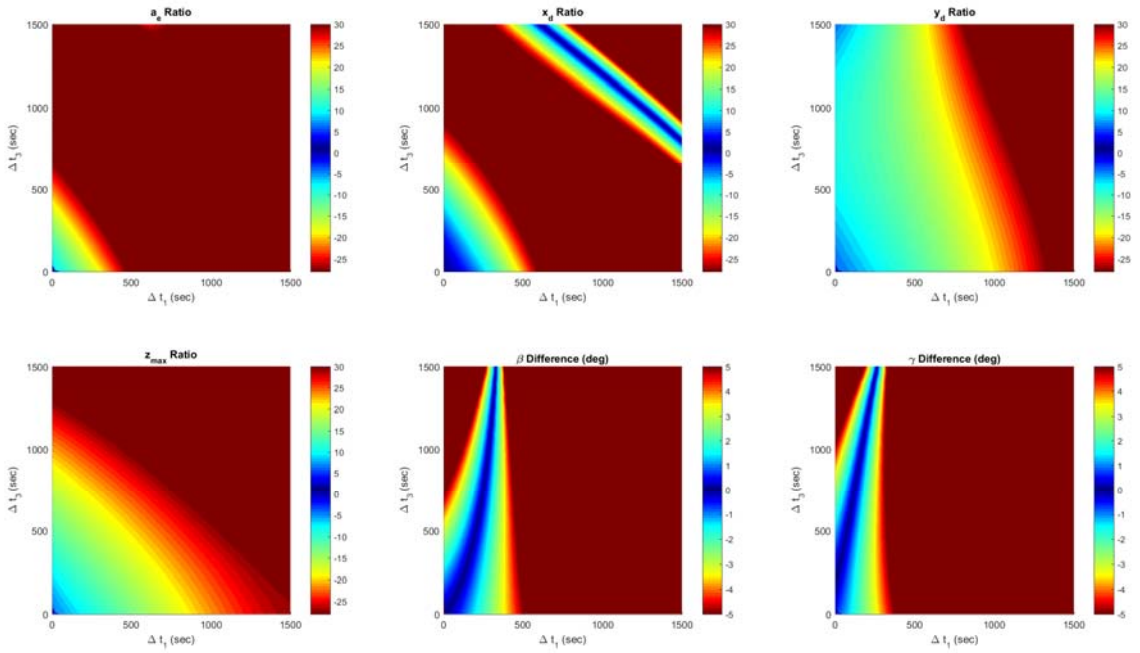

Figure 26. Gauss with Gibbs Velocity Relative Orbital Element Ratios and Differences, Williamsburg Scenario

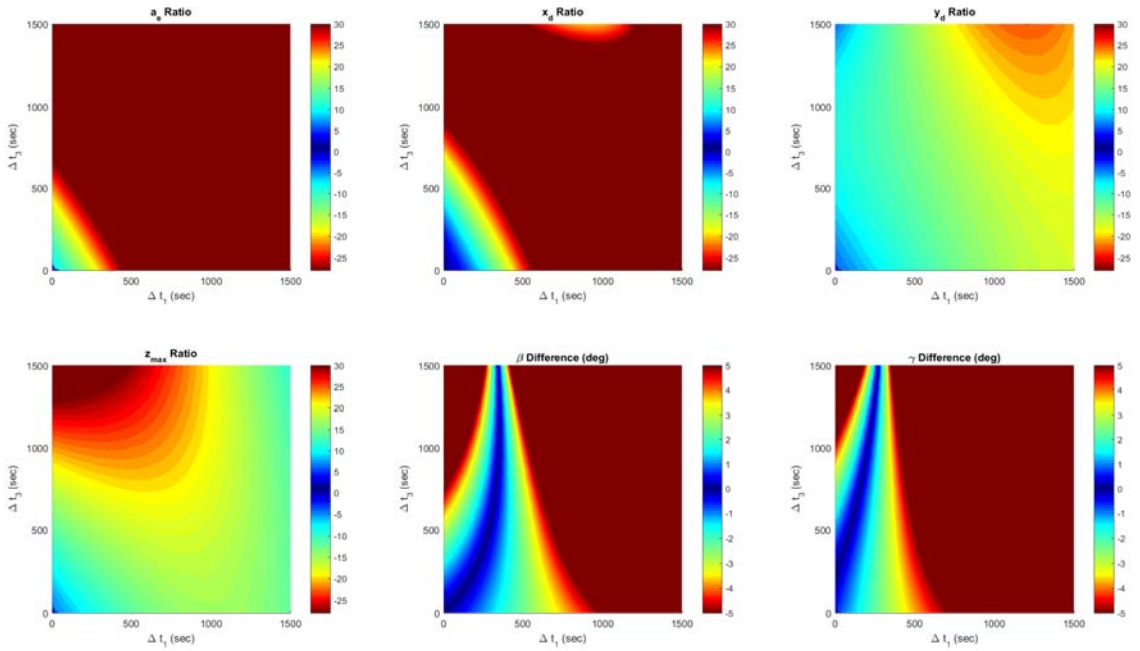

Figure 27. Gauss with Herrick Gibbs Velocity Relative Orbital Element Ratios and Differences, Williamsburg Scenario

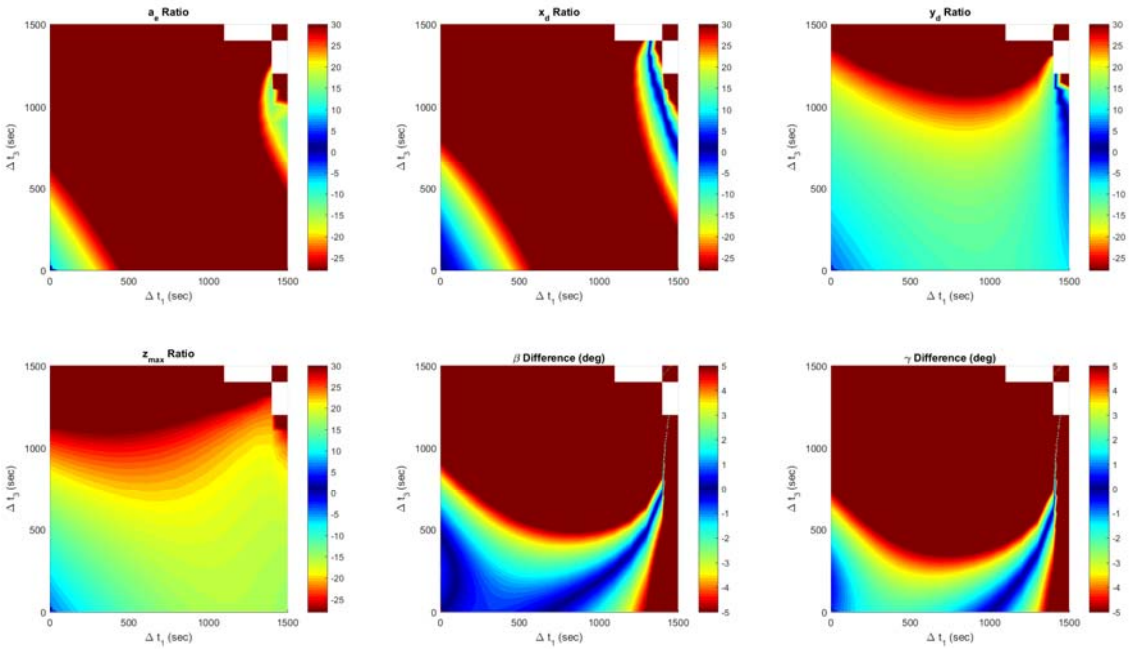

Figure 28. Gauss with Truncated F and G Series Velocity Relative Orbital Element Ratios and Differences, Williamsburg Scenario

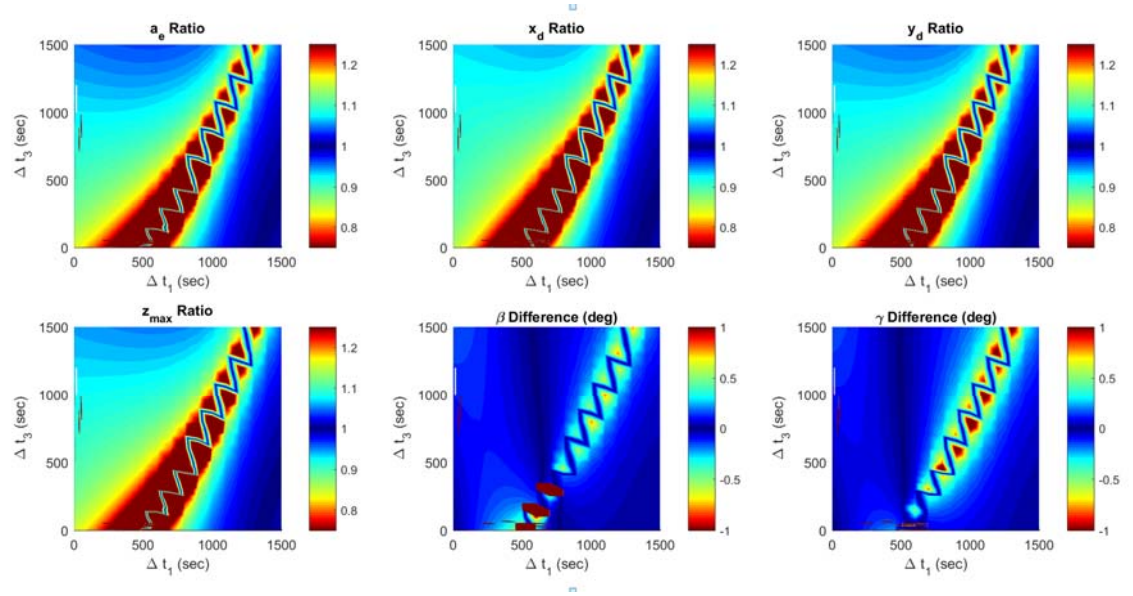

Figure 29. Second Order Relative Orbital Element Ratios and Differences, Williamsburg Scenario

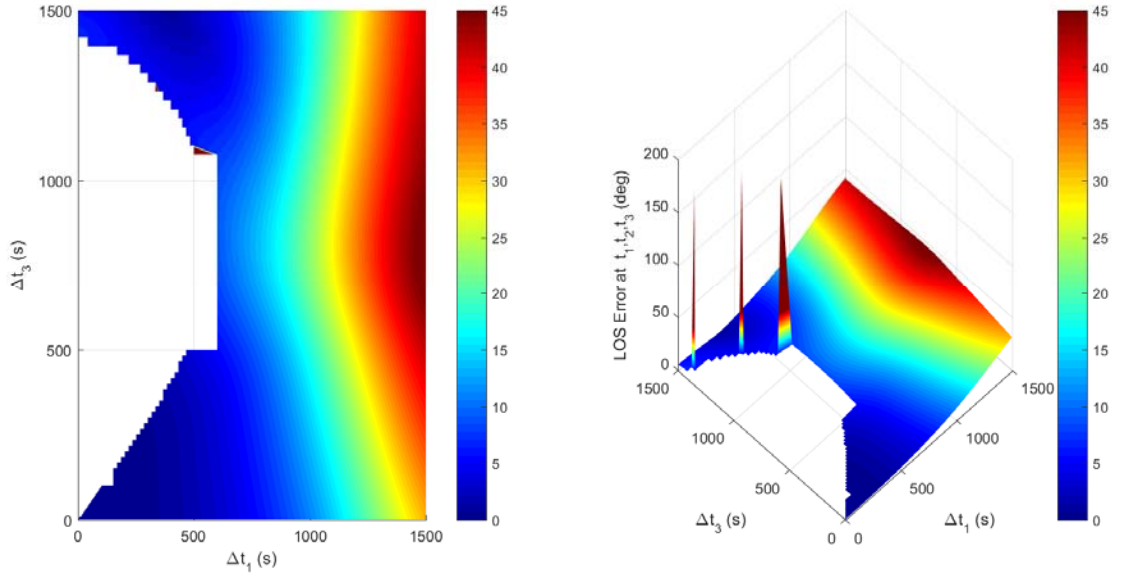

Figure 30. Laplace Line-of-Sight Residuals (deg), 200x100 Ellipse Scenario

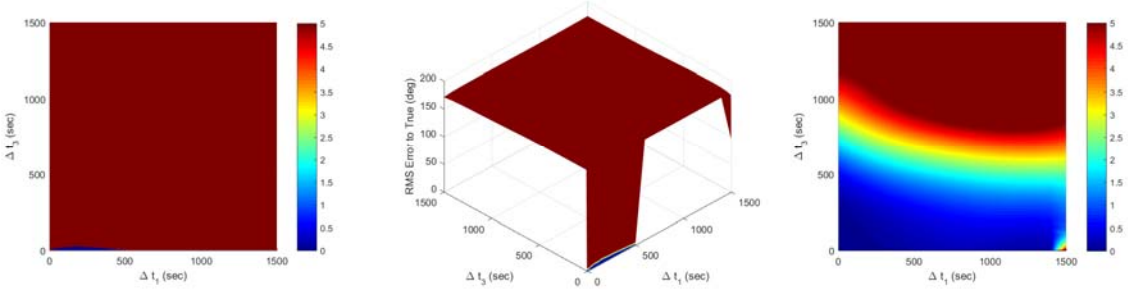

Figure 31. Gauss with Gibbs Velocity Line-of-Sight Residuals (deg), 200x100 Ellipse Scenario

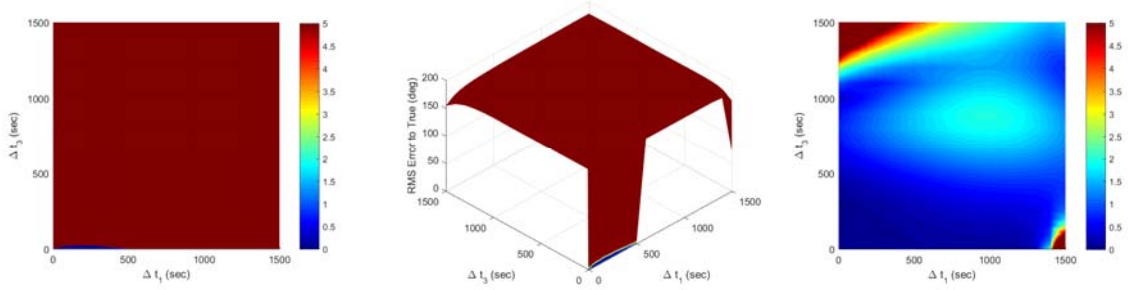

Figure 32. Gauss with Herrick Gibbs Velocity Line-of-Sight Residuals (deg), 200x100 Ellipse Scenario

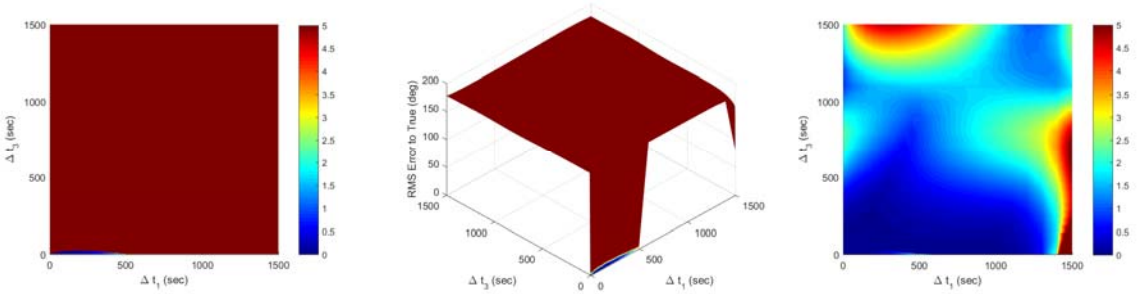

Figure 33. Gauss with Truncated F and G Series Velocity Line-of-Sight Residuals (deg), 200x100 Ellipse Scenario

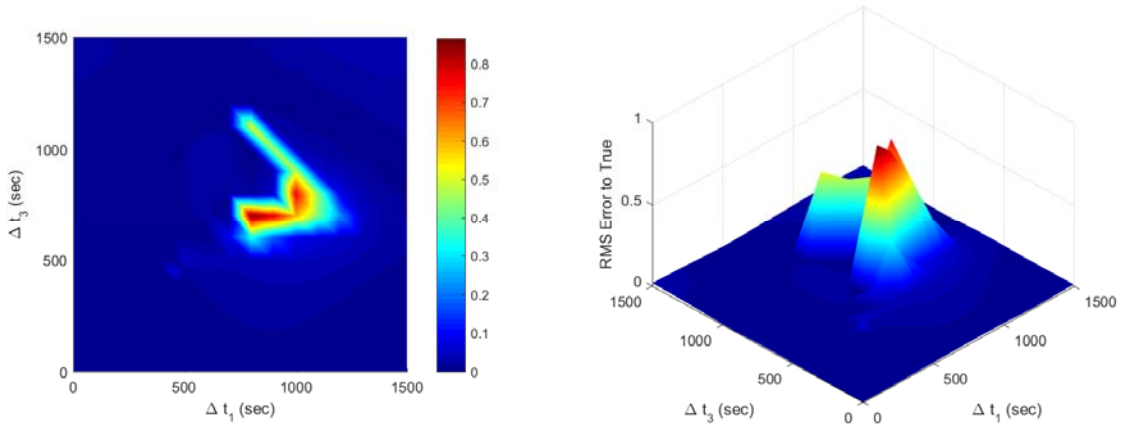

Figure 34. Second Order Line-of-Sight Residuals (deg), 200x100 Ellipse Scenario

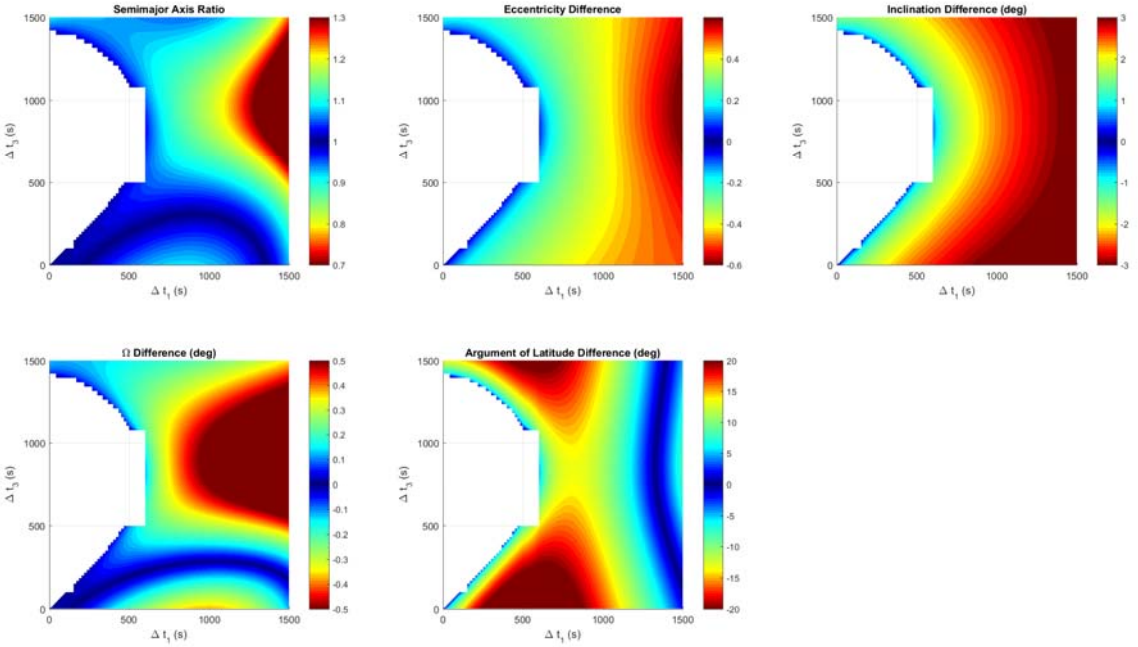

Figure 35. Laplace Orbital Element Ratios and Differences, 200x100 Ellipse Scenario

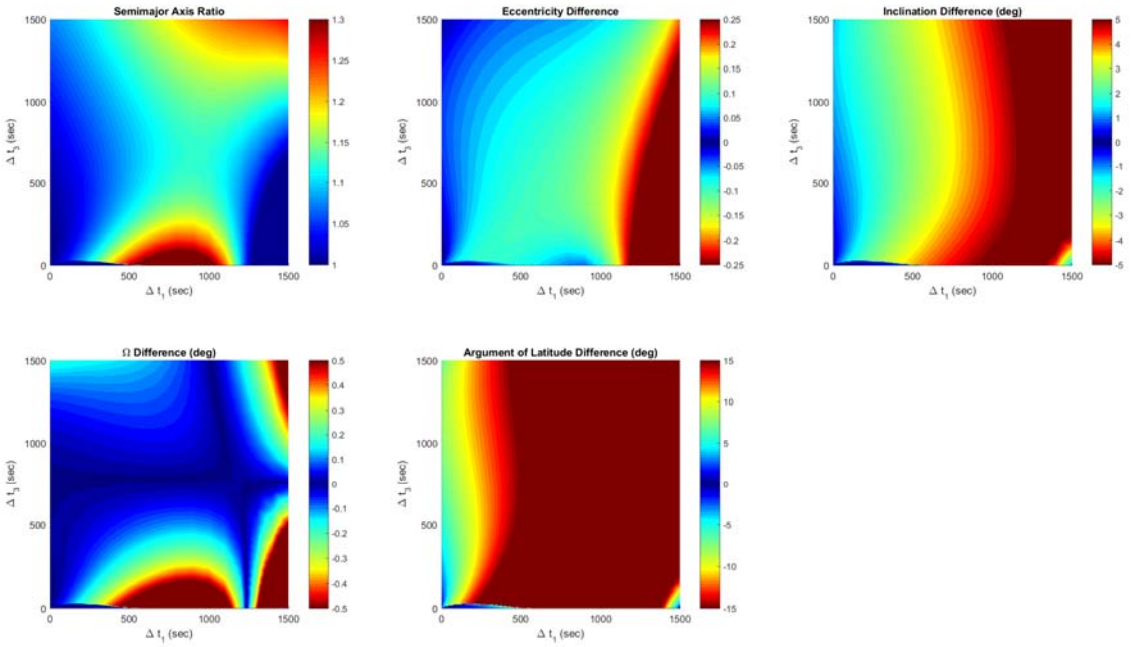

Figure 36. Gauss with Gibbs Velocity Orbital Element Ratios and Differences, 200x100 Ellipse Scenario

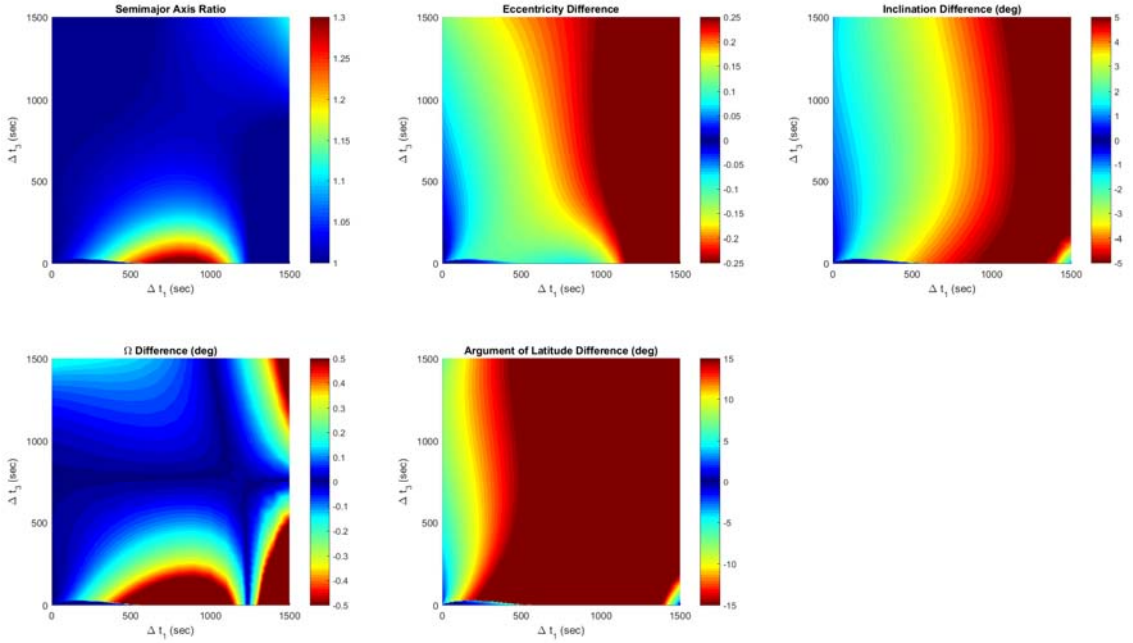

Figure 37. Gauss with Herrick Gibbs Velocity Orbital Element Ratios and Differences, 200x100 Ellipse Scenario

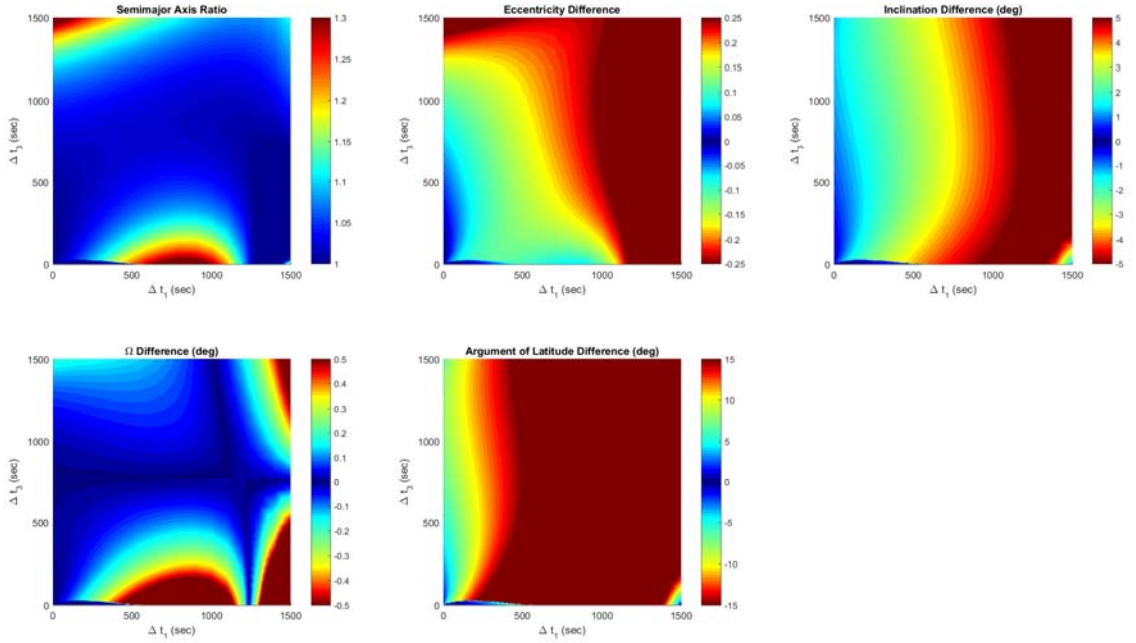

Figure 38. Gauss with Truncated F and G Series Velocity Orbital Element Ratios and Differences, 200x100 Ellipse Scenario

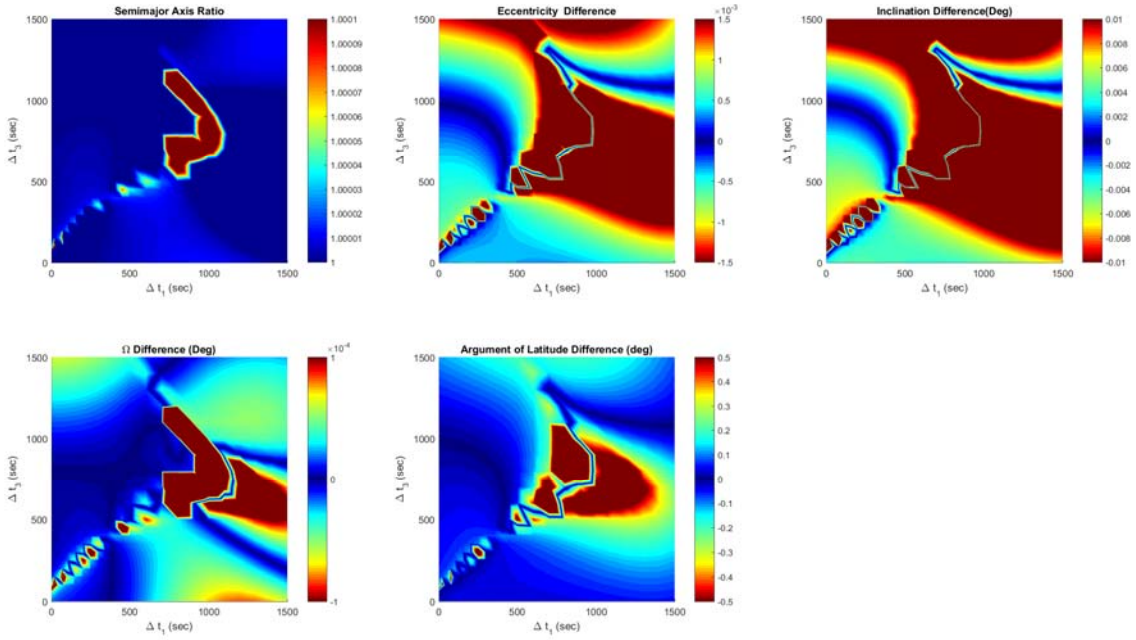

Figure 39. Second Order Orbital Element Ratios and Differences, 200x100 Ellipse Scenario

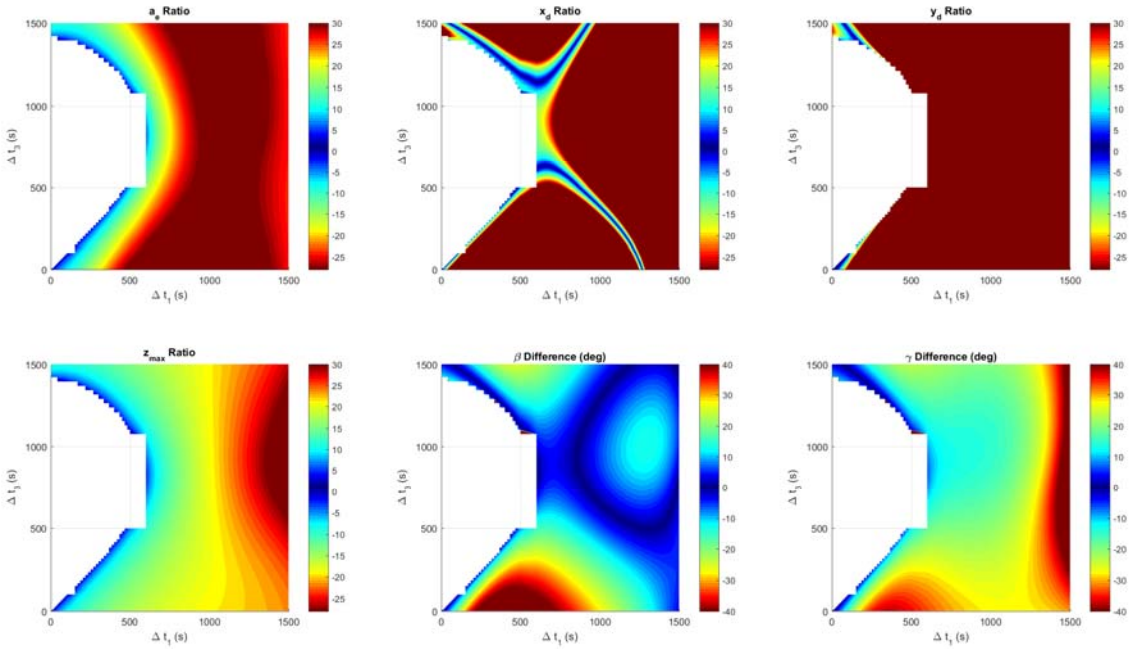

Figure 40. Laplace Relative Orbital Element Ratios and Differences, 200x100 Ellipse Scenario

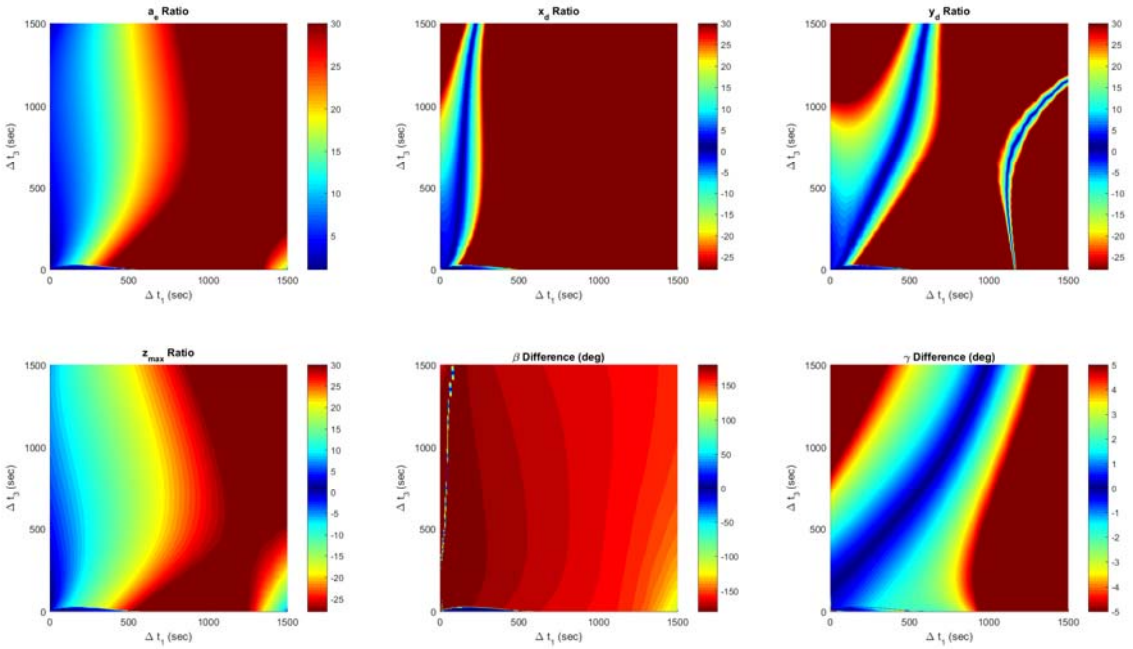

Figure 41. Gauss with Gibbs Velocity Relative Orbital Element Ratios and Differences, 200x100 Ellipse Scenario

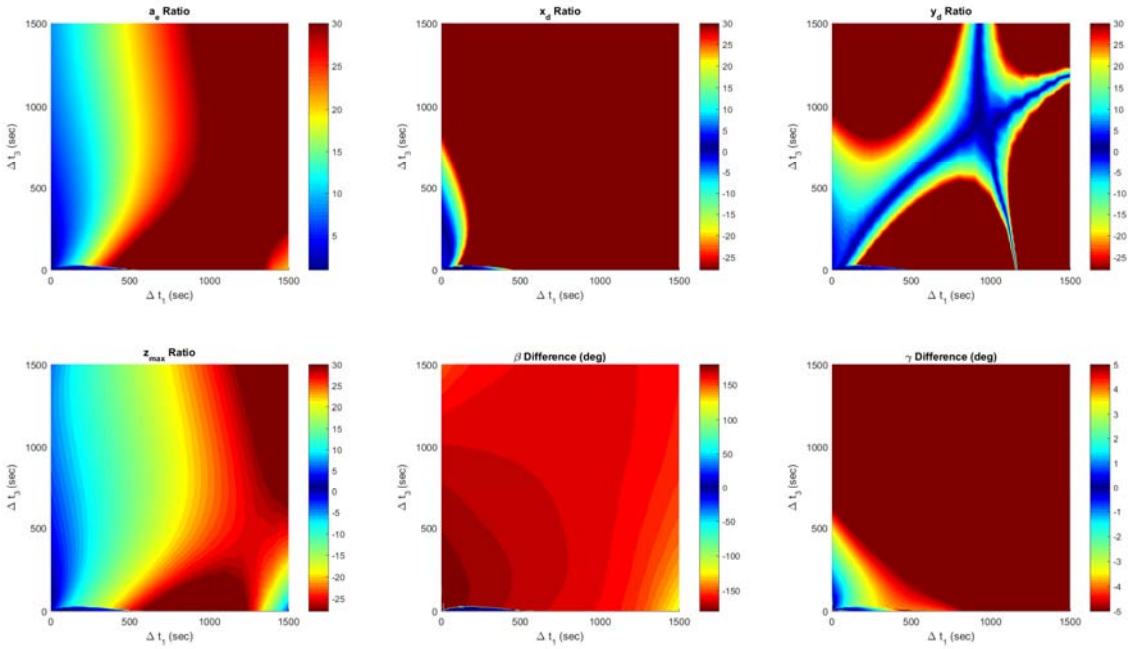

Figure 42. Gauss with Herrick Gibbs Velocity Relative Orbital Element Ratios and Differences, 200x100 Ellipse Scenario

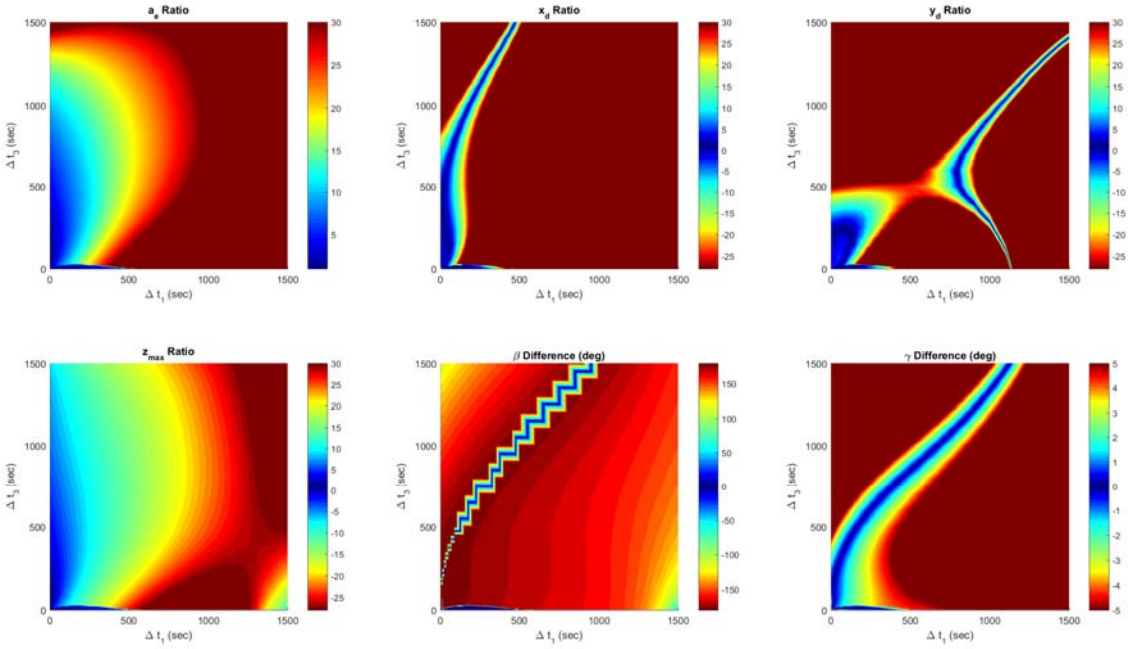

Figure 43. Gauss with Truncated F and G Series Velocity Relative Orbital Element Ratios and Differences, 200x100 Ellipse Scenario

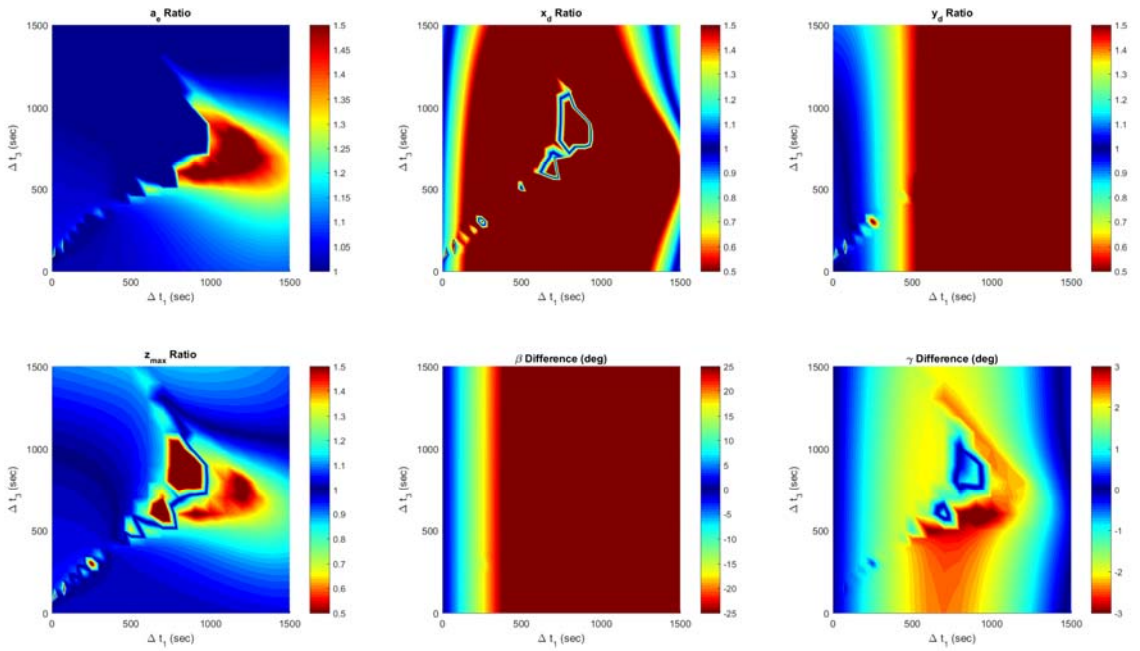

Figure 44. Second Order Relative Orbital Element Ratios and Differences, 200x100 Ellipse Scenario

CONCLUSIONS

This paper has explored the problem of angles-only initial orbit determination from a space-based observer using both classical methods based on inertial orbital dynamics (Laplace and Gauss) and a modern method based on relative orbital dynamics. Results show that the relative technique generally outperforms the classical methods for the simulated examples chosen. Other trends revealed in the results include the relative dependence of the various methods on the choice of measurement times, as well as the classical methods' lack of ability to yield a viable solution in some cases. The results also demonstrate the weak observability of the size (magnitude) of the relative orbit in such scenarios, compared to other aspects of the relative orbit (e.g. shape), regardless of the chosen method.

FUTURE WORK

Planned extensions of this research include:

- A full error analysis of each method, perhaps with the same scenarios above, but involving error introduced into the measurements and the observer's orbit
- Measurement generation with higher fidelity propagation beyond two-body dynamics
- Comparing additional metrics, including computational run-time

REFERENCES

1. P. R. Escobal, Methods of Orbit Determination. Wiley, 1965.
2. Curtis, H. D., Orbital Mechanics for Engineering Students, Elsevier, 2010.

3. Vallado, D. A., Fundamentals of Astrodynamics and Applications, Microcosm Press/Springer, 2007.

4. Tschauner, J. F. A., and Hempel, P. R., “Rendezvous zu einem in elliptischer Bahn umlaufenden Ziel,” Astronautica Acta, Vol. 11, No. 2, 1965, pp. 104–109

5. Clohessy, W. H., and Wiltshire, R. S., "Terminal Guidance System for Satellite Navigation." Journal of Aerospace Sciences 29, pp. 653-658, 1960

6. London, H. S., “Second Approximation to the Solution of the Rendezvous Equations,” AIAA Journal, Vol. 1, No. 7, 1963, pp. 1691–1693

7. Anthony, M. L. and Sasaki, F. T., “Rendezvous Problem for Nearly Circular Orbits,” AIAA Journal, Vol. 3, No. 7, 1965, pp. 1666–1673

8. Newman, B. A., and Lovell, T. A., “Second Order Nonlinear Boundary Value Solution for Relative Motion Using Volterra Theory,” AAS Paper 13-470, presented at the AAS/AIAA Space Flight Mechanics Meeting, Kauai, HI, Feb 10-14, 2013

9. B. Newman, T. A. Lovell, E. Pratt and E. Duncan, “Quadratic Hexa-Dimensional Solution for Relative Orbit Determination – Revisited," AAS/AIAA Space Flight Mechanics Meeting, Williamsburg, Virginia, January 2015, AAS Paper 15-398

10. Sinclair, A. J., Lovell, T. A., Horneman, K. R., Harris, A. T., Sizemore, A. E., “Relative-Motion Approach for Differential Correction in Orbit Determination”, AAS Paper 17-327, presented at the AAS/AIAA Space Flight Mechanics Meeting, San Antonio, Texas, 9-13 February 2017

11. Lovell, T.A., and Tragesser, S.G., “Guidance for Relative Motion of Low Earth Orbit Spacecraft Based on Relative Orbit Elements,” AIAA Paper 2004-4988, presented at the AAS/AIAA Astrodynamics Specialist Conference, Providence, RI, Aug 16-19, 2004

12. Lovell, T.A., and Spencer, D.A., “Relative Orbital Elements Formulation Based upon the Clohessy-Wiltshire Equations,” Journal of the Astronautical Sciences, December 2014, Volume 61, Issue 4, pp 341-366

13. Woffinden, D., Angles-Only Navigation for Autonomous Orbital Rendezvous. PhD thesis, Utah State University, Logan, Utah, Aug. 2008Newman, Lovell, Pratt, and Duncan, “Quadratic Hexa-Dimensional Solution for Relative Orbit Determination - Revisit-ed,” AAS Paper 15-398, presented at the AAS/AIAA Space Flight Mechanics Meeting, Williamsburg, VA, Jan 11-15, 2015

14. Bates, D. J., Hauenstein, J. D., Sommese, A. J., and Wampler, C. W. Numerically solving polynomial systems with Bertini. SIAM, 2013

15. Kirwan, F., Complex Algebraic Curves, Cambridge University Press, Cambridge, England, 1992